

# DRAFT

## CMS Paper

*The content of this note is intended for CMS internal use and distribution only*

2024/03/22

Archive Hash: af06c7c-D

Archive Date: 2024/03/22

### Observation of $\gamma\gamma \rightarrow \tau\tau$ in proton-proton collisions and limits on the anomalous electromagnetic moments of the $\tau$ lepton

The CMS Collaboration

#### Abstract

The photon-induced production of a pair of  $\tau$  leptons,  $\gamma\gamma \rightarrow \tau\tau$ , is observed for the first time in proton-proton collisions. The observation is based on a data set recorded with the CMS detector at the LHC at a center-of-mass energy of 13 TeV and corresponding to an integrated luminosity of  $138 \text{ fb}^{-1}$ . Events with a small number of tracks close to the di- $\tau$  vertex are selected to isolate photon-induced processes. Limits on the anomalous electromagnetic moments of the  $\tau$  lepton originating from potential new physics effects on the  $\gamma\tau\tau$  vertex are also set.

This box is only visible in draft mode. Please make sure the values below make sense.

PDFAuthor: Cecile Caillol  
PDFTitle: Observation of gammagamma to tautau in proton-proton collisions and limits on the anomalous electromagnetic moments of the tau lepton  
PDFSubject: CMS  
PDFKeywords: CMS, exclusive production, taus

Please also verify that the abstract does not use any user defined symbols



# 1 Introduction

The production of lepton pairs in photon-induced interactions draws significant interest since it is a pure quantum electrodynamics (QED) process, for which the cross section is known with a high level of accuracy. This process is characterized by its color-neutral nature, leading to low hadronic activity, and was first measured by the CMS Collaboration in the dielectron and dimuon final states [1, 2]. Although the photon-lepton vertex is measured up to high precision for electrons and muons, the couplings to  $\tau$  leptons lack a similar experimental precision.

The most general form of photon-lepton vertex ( $ie\Gamma^\mu$ ) satisfying Lorentz invariance is:

$$\Gamma^\mu = \gamma^\mu F_1(q^2) + \frac{\sigma^{\mu\nu} q_\nu}{2m} [iF_2(q^2) + F_3(q^2) \gamma_5], \quad (1)$$

where  $F_1$ ,  $F_2$  and  $F_3$  are form factors that contain the complete information about the lepton's gross electric and magnetic couplings. Beyond serving as a deep test of QED interactions, the photon-lepton vertex also offers insights into the anomalous electromagnetic moments of the lepton,  $F_2(0) = a_\ell \equiv (g_\ell - 2)/2$  and  $F_3(0) = -\frac{2m}{e}d_\ell$ , and is a powerful probe of physics beyond the standard model (BSM). In this expression, the gyromagnetic ratio  $g_\ell$  is a constant term that relates the magnetic moment to the spin of the lepton. The one-loop contribution to  $a_\ell$  is equal to the so-called "Schwinger term" [3]:

$$a_\ell = \frac{\alpha}{2\pi} \simeq 0.00116, \quad (2)$$

where  $\alpha$  is the fine-structure constant.

The anomalous magnetic moment of the electron was measured to be in agreement with the standard model (SM) with an impressive precision of 12 significant digits [4, 5], whereas a tension of about 4 standard deviations (s.d.) with respect to the theoretical prediction was observed by the Muon g-2 Collaboration when measuring  $a_\mu$  [6, 7]. If BSM effects scale with the squared lepton mass [8], deviations of  $a_\tau$  from the SM predictions would be more than two orders of magnitude larger. The photon-induced production of a  $\tau$  lepton pair involves  $\tau\tau\gamma$  vertices and can be used to measure  $a_\tau$ , which, in the SM, is predicted to be  $a_\tau = 117721(5) \times 10^{-8}$  [9]. This same process can also be studied to constrain the electric dipole moment (EDM) of the  $\tau$  lepton,  $d_\tau$ , which, since there is no appreciable CP violation in the lepton sector in the SM [10], is predicted to have a nonzero but tiny value ( $d_\tau = -7.3 \times 10^{-38} e \text{ cm}$ ).

The signal in this analysis is  $pp(\gamma\gamma) \rightarrow p^{(*)}\tau^+\tau^-p^{(*)}$ , where  $p^{(*)}$  denotes a final state proton that stays intact or fragments after the photon emission. In the following, charges will be omitted from the notations for simplicity. When coherent photon radiation happens without proton dissociation for both photons, the process is called exclusive or elastic. Elastic photon emissions force the photons to be almost on-shell, limiting their virtuality to small values ( $q^2 \rightarrow 0$ ) [11]. When one or two photons are radiated off a parton of the proton, the process is either single-dissociative or double-dissociative. The three diagrams are shown in Fig. 1. Single-dissociative and double-dissociative events can also give rise to an elastic-like signature when the proton remnants are not reconstructed because they fall outside of the detector acceptance.

The  $\gamma\gamma \rightarrow \tau\tau$  process has been observed by the ATLAS and CMS experiments in ultraperipheral collisions of nuclei [12, 13], and further used to set constraints on  $a_\tau$ . The observation was driven by signal events with a di- $\tau$  invariant mass,  $m_{\tau\tau}$ , typically below 20 GeV. This paper describes the first measurement of the photon-induced production of a pair of  $\tau$  leptons in proton-proton (pp) collisions. Because of the trigger requirements, experimentally accessible

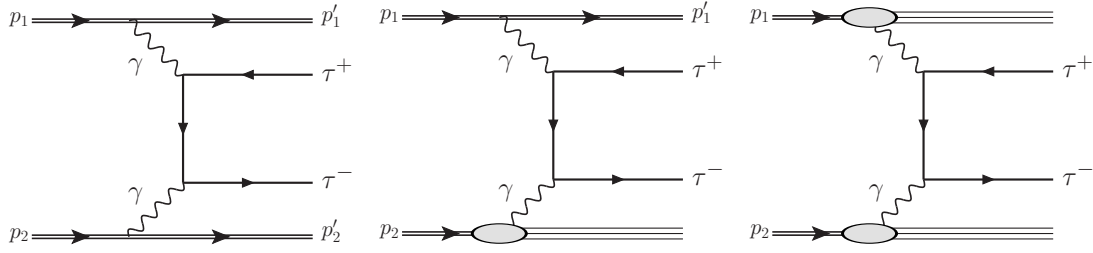


Figure 1: Production of  $\tau$  lepton pairs by  $\gamma\gamma$  fusion. The exclusive (left), single proton dissociation or semiexclusive (middle), and double proton dissociation (right) topologies are shown.

signal events have  $m_{\tau\tau} > 50$  GeV. This phase space has a much lower cross section, but the integrated luminosity is higher than that of the heavy ion runs. Additionally, BSM effects are enhanced at high mass, such that constraints on BSM scenarios with non-SM  $a_\tau$  and  $d_\tau$  values can be set using both the rate of the signal and its  $m_{\tau\tau}$  distribution. Outside of LHC experiments, constraints on  $a_\tau$  were previously set by the DELPHI, OPAL, and L3 experiments [14–16]. The best constraint on  $d_\tau$  comes from the Belle experiment [17], while the ARGUS, OPAL, and L3 Collaborations also determined confidence intervals [15, 16, 18].

This paper presents the first observation of the  $\gamma\gamma \rightarrow \tau\tau$  process in pp collision events, as well as constraints on  $a_\tau$  and  $d_\tau$ . It is based on pp collision data at  $\sqrt{s} = 13$  TeV collected with the CMS detector in 2016–2018 and corresponding to an integrated luminosity of  $138 \text{ fb}^{-1}$ . To select the signal, we apply so-called exclusivity criteria, which rely on the geometry of the di- $\tau$  system and on the activity in the tracker part of the detector around the di- $\tau$  vertex. In particular, selecting events with no track around the di- $\tau$  vertex can reduce the backgrounds by about three orders of magnitude for a signal efficiency around 50%. Such a strategy was used recently by the ATLAS experiment to observe  $\gamma\gamma \rightarrow WW$  events in pp collisions [19], and in earlier searches and measurements at the LHC [2, 20–23]. Four different final states are used to extract the signal, depending on the decay of the  $\tau$  lepton:  $e\mu$ ,  $e\tau_h$ ,  $\mu\tau_h$ , and  $\tau_h\tau_h$ , where  $\tau_h$  denotes a  $\tau$  lepton decaying hadronically. Events with two reconstructed muons are also used to derive corrections to the simulated samples. The visible mass of the  $\tau$  candidates,  $m_{\text{vis}}$ , computed as the invariant mass of the visible decay products of the  $\tau$  leptons, is used as a biased estimator of  $m_{\tau\tau}$  to extract the significance of the signal and constraints on  $a_\tau$  and  $d_\tau$ .

## 2 The CMS detector

The central feature of the CMS apparatus is a superconducting solenoid of 6 m internal diameter, providing a magnetic field of 3.8 T. Within the solenoid volume are a silicon pixel and strip tracker, a lead tungstate crystal magnetic calorimeter (ECAL), and a brass and scintillator hadron calorimeter (HCAL), each composed of a barrel and two endcap sections. Forward calorimeters extend the pseudorapidity coverage provided by the barrel and endcap detectors. Muons are measured in gas-ionization detectors embedded in the steel flux-return yoke outside the solenoid. A more detailed description of the CMS detector, together with a definition of the coordinate system used and the relevant kinematic variables, can be found in Ref. [24].

Events of interest are selected using a two-tiered trigger system. The first level (L1), composed of custom hardware processors, uses information from the calorimeters and muon detectors to select events at a rate of around 100 kHz within a fixed latency of about  $4 \mu\text{s}$  [25]. The second level, known as the high-level trigger (HLT), consists of a farm of processors running a version of the full event reconstruction software optimized for fast processing, and reduces the event rate to around 1 kHz before data storage [26].

### 3 Signal and background modeling

Signal samples corresponding to the elastic photon-induced production of a  $\tau$  lepton pair are generated using the GAMMA-UPC generator [27], which handles final states produced via photon fusion incorporated in MADGRAPH5\_aMC@NLO v3.5 [28–30]. Photon fluxes are derived from the integral over the charge form factors of the nucleus. The SUPERCHIC 4 generator [31] is used as a cross check, as described in Section 7.

In this analysis,  $a_\tau$  and  $d_\tau$  are parameterized using the SMEFTsim package [32, 33], as suggested in Ref. [8]. The corresponding BSM Lagrangian in the SM effective field theory (SMEFT) approach consists of two dimension-6 operators modifying  $a_\tau$  and  $d_\tau$  at tree level:

$$\mathcal{L}_{\text{BSM}} = \frac{C_{\tau B}}{\Lambda^2} \bar{L}_L \sigma^{\mu\nu} \tau_R H B_{\mu\nu} + \frac{C_{\tau W}}{\Lambda^2} \bar{L}_L \sigma^{\mu\nu} \tau_R \sigma^i H W_{\mu\nu}^i + \text{h.c.}, \quad (3)$$

where  $\Lambda$  is the scale of BSM physics and  $C_{\tau B}$  and  $C_{\tau W}$  are Wilson coefficients. Using the *SMEFTsim\_general\_alphaScheme\_UFO* model, after electroweak symmetry breaking, the  $\tau\tau\gamma$  vertex is parameterized as:

$$V_{\tau\tau\gamma} = ie\gamma^\mu - \frac{v\sqrt{2}}{\Lambda^2} \left[ \text{Re}[C_{\tau\gamma}] + \text{Im}[C_{\tau\gamma}] i\gamma_5 \right] \sigma^{\mu\nu} q_\nu, \quad (4)$$

where  $v$  is equal to 246 GeV,  $C_{\tau\gamma} = (\cos\theta_W C_{\tau B} - \sin\theta_W C_{\tau W})$ , and  $\theta_W$  is the Weinberg angle. Using Eq. (1) and Eq. (4), the BSM contributions to  $a_\tau$  and  $d_\tau$  can be expressed as:

$$\delta a_\tau = \frac{2m_\tau}{e} \frac{\sqrt{2}v}{\Lambda^2} \text{Re}[C_{\tau\gamma}] \quad (5)$$

and

$$\delta d_\tau = \frac{\sqrt{2}v}{\Lambda^2} \text{Im}[C_{\tau\gamma}]. \quad (6)$$

For simplicity and without loss of generality since  $\delta a_\tau$  and  $\delta d_\tau$  only depend on  $C_{\tau\gamma}$  and not on the individual values of  $C_{\tau W}$  and  $C_{\tau B}$ , we set  $C_{\tau W}$  to 0 in the signal simulation. BSM contributions to the  $Z \rightarrow \tau\tau$  vertex cancel for  $C_{\tau W} = -\tan\theta_W C_{\tau B}$ , but other values of  $C_{\tau W}$  would result in variations in the Drell–Yan process prediction that are negligible with respect to the systematic uncertainties in this analysis. The simulation of different anomalous electromagnetic moments is performed using a matrix element reweighting [34], scanning over a range of  $C_{\tau B}$  values. In the simulation we set  $\Lambda$  to 2 TeV, but the results were checked not to depend on the scale of new physics for  $\Lambda > 0.5$  TeV. As the anomalous electromagnetic moments of the  $\tau$  lepton depend on  $C_{\tau W}/\Lambda^2$  and  $C_{\tau B}/\Lambda^2$ , the analysis results can also be interpreted in this two-dimensional plane.

Single-dissociative and double-dissociative processes are not simulated but estimated from data as described later. The same generator is used to simulate the elastic photon-induced production of pairs of electrons, muons, and W bosons, which are backgrounds in the signal region (SR).

The MADGRAPH5\_aMC@NLO 2.6.5 event generator is used to generate events originating from the  $Z/\gamma^* + \text{jets}$  and  $W + \text{jets}$  processes, as well as from the diboson production with two leptons and two neutrinos in the final state. They are simulated at next-to-leading order (NLO) with the FxFx jet matching and merging [30]. The MADGRAPH5\_aMC@NLO generator is also used for the simulation of the minor contribution from other diboson production events, whereas

POWHEG 2.0 [35–39] is used for  $t\bar{t}$  and single top quark production. The generators are interfaced with PYTHIA 8.240 [40] to model the parton showering, fragmentation, and hadronization, as well as the decay of the  $\tau$  leptons. The PYTHIA parameters affecting the description of the underlying event are set to the CP5 tune [41]. The NNPDF3.1 parton distribution function (PDF) set [42–44] at next-to-NLO (NNLO) accuracy is used for background simulations. Additional pp interactions per bunch crossing (pileup, PU) are added to the simulated samples with a distribution that is chosen to match that observed in the data. Generated events are processed through a GEANT4 [45] simulation of the CMS detector.

## 4 Object reconstruction

The global event reconstruction (also called particle-flow event reconstruction [46]) aims to reconstruct and identify each individual particle in an event, with an optimized combination of all subdetector information. In this process, the identification of the particle type (photon, electron, muon, charged hadron, neutral hadron) plays an important role in the determination of the particle direction and energy. Photons (e.g., coming from  $\pi^0$  decays or from electron bremsstrahlung) are identified as ECAL energy clusters not linked to the extrapolation of any charged particle trajectory to the ECAL. Electrons (e.g., coming from photon conversions in the tracker material or from B hadron semileptonic decays) are identified as a primary charged particle track and potentially many ECAL energy clusters corresponding to this track extrapolation to the ECAL and to possible bremsstrahlung photons emitted along the way through the tracker material. Muons (e.g., from B hadron semileptonic decays) are identified as tracks in the central tracker consistent with either a track or several hits in the muon system, and associated with calorimeter deposits compatible with the muon hypothesis. Charged hadrons are identified as charged particle tracks neither identified as electrons, nor as muons. Finally, neutral hadrons are identified as HCAL energy clusters not linked to any charged hadron trajectory, or as a combined ECAL and HCAL energy excess with respect to the expected charged hadron energy deposit.

The electron momentum is estimated by combining the energy measurement in the ECAL with the momentum measurement in the tracker. The momentum resolution for electrons with transverse momentum  $p_T \approx 45$  GeV from  $Z \rightarrow ee$  decays ranges from 1.6 to 5%. It is generally better in the barrel region than in the endcaps, and also depends on the bremsstrahlung energy emitted by the electron as it traverses the material in front of the ECAL [47, 48].

Muons are measured in the pseudorapidity range  $|\eta| < 2.4$ , with detection planes made using three technologies: drift tubes, cathode strip chambers, and resistive plate chambers. The single muon trigger efficiency exceeds 90% over the full  $\eta$  range, and the efficiency to reconstruct and identify muons is greater than 96%. Matching muons to tracks measured in the silicon tracker results in a relative  $p_T$  resolution, for muons with  $p_T$  up to 100 GeV, of 1% in the barrel and 3% in the endcaps. The  $p_T$  resolution in the barrel is better than 7% for muons with  $p_T$  up to 1 TeV [49].

Hadronic  $\tau$  decays ( $\tau_h$ ) are reconstructed from jets, using the hadrons-plus-strips algorithm [50], which combines 1 or 3 tracks with energy deposits in the calorimeters. Neutral pions are reconstructed as strips with dynamic size in  $\eta$ - $\phi$  from reconstructed electrons and photons, where the strip size varies as a function of the  $p_T$  of the electron or photon candidate. The  $\tau_h$  are reconstructed in four possible decay modes (DMs): a single charged hadron ( $h^\pm$ ), a charged hadron with at least one neutral pion ( $h^\pm + \pi^0(s)$ ), three charged hadrons with no neutral pion ( $h^\pm h^\mp h^\pm$ ), or 3 charged hadrons with at least one neutral pion ( $h^\pm h^\mp h^\pm + \pi^0(s)$ ). To distinguish genuine  $\tau_h$  decays from jets originating from the hadronization of quarks or gluons, and from



electrons, or muons, the DEEPTAU algorithm is used [51]. Information from all individual reconstructed particles near the  $\tau_h$  axis is combined with properties of the  $\tau_h$  candidate and the event. The rate of a jet to be misidentified as  $\tau_h$  by the DEEPTAU algorithm depends on the  $p_T$  and quark flavor of the jet. In simulated events from W boson production in association with jets it has been estimated to be 0.43% for a genuine  $\tau_h$  identification efficiency of 70%. The misidentification rate for electrons (muons) is 2.60 (0.03)% for a genuine  $\tau_h$  identification efficiency of 80 (>99)%.

The missing transverse momentum vector  $\vec{p}_T^{\text{miss}}$  is computed as the negative vector sum of the transverse momenta ( $p_T$ ) of all the PF candidates in an event, and its magnitude is denoted as  $p_T^{\text{miss}}$  [52]. The  $\vec{p}_T^{\text{miss}}$  is modified to account for corrections to the energy scale of the reconstructed jets in the event. Anomalous high- $p_T^{\text{miss}}$  events can be due to a variety of reconstruction failures, detector malfunctions or noncollision backgrounds. Such events are rejected by event filters that are designed to identify more than 85–90% of the spurious high- $p_T^{\text{miss}}$  events with a mistagging rate less than 0.1% [52].

Tracks with  $p_T > 0.5$  GeV and  $|\eta| < 2.5$  are used in this analysis to measure the hadronic activity in the event. The silicon tracker used in 2016 measured charged particles within the range  $|\eta| < 2.5$ . For nonisolated particles of  $1 < p_T < 10$  GeV and  $|\eta| < 1.4$ , the track resolutions were typically 1.5% in  $p_T$  and 25–90 (45–150)  $\mu\text{m}$  in the transverse (longitudinal) impact parameter [53]. At the start of 2017, a new pixel detector was installed [54]; the upgraded tracker measured particles up to  $|\eta| < 3.0$  with typical resolutions of 1.5% in  $p_T$  and 20–75  $\mu\text{m}$  in the transverse impact parameter [55] for nonisolated particles of  $1 < p_T < 10$  GeV.

During the 2016 and 2017 data-taking, a gradual shift in the timing of the inputs of the ECAL L1 trigger in the region at  $|\eta| > 2.0$  caused a specific trigger inefficiency. For events containing an electron (a jet) with  $p_T$  larger than  $\approx 50$  GeV ( $\approx 100$  GeV), in the region  $2.5 < |\eta| < 3.0$  the efficiency loss is  $\approx 10$ –20%, depending on  $p_T$ ,  $\eta$ , and time. Correction factors were computed from data and applied to the acceptance evaluated by simulation.

## 5 Event selection

Events in the SR are selected in the  $e\mu$ ,  $e\tau_h$ ,  $\mu\tau_h$ , and  $\tau_h\tau_h$  final states, which account for 94% of the possible final states with a pair of  $\tau$  leptons. The  $\mu\mu$  final state is used to derive the following corrections:

- a correction to the pileup track density in all simulations, described in Section 6.1;
- a correction to the hard scattering track multiplicity in the Drell–Yan and diboson simulations, described in Section 6.2;
- a correction to the elastic photon-induced simulations to include dissociative contributions, described in Section 7;
- a correction to the acoplanarity distribution in the Drell–Yan simulation, described in Section 8.1.

In the  $e\mu$  final state, events are triggered with a combination of triggers requiring an electron and a muon, with a  $p_T$  threshold of 23 GeV for the leading lepton, and 8 or 12 GeV for the subleading lepton if it is a muon or an electron, respectively. Offline, the leading lepton is required to have  $p_T > 24$  GeV and the subleading lepton  $p_T > 15$  GeV. The subleading lepton  $p_T$  threshold is several GeV above the trigger  $p_T$  thresholds to reduce background processes with misidentified jets. In the  $e\tau_h$  ( $\mu\tau_h$ ) final states, events are triggered with single electron (muon) triggers with  $p_T$  thresholds ranging between 25 and 32 (24 and 27) GeV depending on

Table 1: Baseline selection criteria used in the different final states of the SR and in the  $\mu\mu$  CR. The electrons, muons, and  $\tau_h$  are required to be well identified and isolated. The  $p_T$  and pseudorapidity ranges correspond to different sets of triggers, and different data-taking periods.

	$e\mu$	$e\tau_h$	$\mu\tau_h$	$\tau_h\tau_h$	$\mu\mu$
$p_T^e$ (GeV)	$> 15/24$	$> 25 - 33$	—	—	—
$ \eta^e $	$< 2.5$	$< 2.1 - 2.5$	—	—	—
$p_T^\mu$ (GeV)	$> 24/15$	—	$> 21 - 29$	—	$> 26 - 29/10$
$ \eta^\mu $	$< 2.4$	—	$< 2.1 - 2.4$	—	—
$p_T^{\tau_h}$ (GeV)	—	$> 30 - 35$	$> 30 - 32$	$> 40$	—
$ \eta^{\tau_h} $	—	$< 2.1 - 2.3$	$< 2.1 - 2.3$	$< 2.1$	—
$m_{\mu\mu}$ (GeV)	—	—	—	—	$> 50$
OS	yes	yes	yes	yes	yes
$ d_z(\ell, \ell') $ (cm)	$< 0.1$	$< 0.1$	$< 0.1$	$< 0.1$	$< 0.1$
$\Delta R(\ell, \ell')$	$> 0.5$	$> 0.5$	$> 0.5$	$> 0.5$	$> 0.5$
$m_T(e/\mu, \vec{p}_T^{\text{miss}})$ (GeV)	—	$< 75$	$< 75$	—	—

the data-taking year. Additional events with lepton  $p_T$  as low as 24 (19) GeV and  $|\eta| < 2.1$  can be selected using cross triggers requiring also the presence of a  $\tau_h$  candidate with  $p_T$  above 20 (27) GeV and  $|\eta| < 2.1$ . In these two final states, the background from  $W + \text{jets}$  is reduced by requiring the transverse mass between the lepton and  $\vec{p}_T^{\text{miss}}$ ,  $m_T(e/\mu, \vec{p}_T^{\text{miss}})$ , to be less than 75 GeV. The events in the  $\tau_h\tau_h$  final state are selected with triggers requiring the presence of two loosely isolated  $\tau_h$  candidates with  $p_T > 35 - 40$  GeV and  $|\eta| < 2.1$ . The offline thresholds are  $p_T > 40$  GeV and  $|\eta| < 2.1$  for all the data-taking periods. A trigger requiring a single muon with  $p_T > 24 - 27$  GeV is used to select events in the  $\mu\mu$  final state. Offline, the leading (subleading) muon is required to have  $p_T > 26 - 29(10)$  GeV and  $|\eta| < 2.4$ . The invariant mass of the two muons,  $m_{\mu\mu}$ , must be greater than 50 GeV.

In all final states, the two objects are required to be well-identified and isolated, to have opposite sign (OS) charge, to be separated from each other by  $\Delta R = \sqrt{(\Delta\eta)^2 + (\Delta\phi)^2} > 0.5$ , and to satisfy  $|d_z(\ell, \ell')| < 0.1$  cm, where  $|d_z(\ell, \ell')|$  is the difference in the longitudinal impact parameters of the two objects. Final states are made mutually exclusive by vetoing events that have additional identified and isolated electrons or muons.

The criteria listed above and summarized in Table 1 constitute the baseline selection, on top of which other requirements can be applied to define the SR or the control regions (CRs) used to derive corrections. In particular, events in the SR are required to have low acoplanarity and track multiplicity, as described in the following paragraphs, in order to improve the signal-to-background ratio using the characteristics of the exclusive process signature.

The acoplanarity, defined as:

$$A = 1 - |\Delta\phi(\ell, \ell')|/\pi, \quad (7)$$

is typically small for photon-induced elastic events, for which the leptons are produced back-to-back. In the case of  $\tau$  leptons,  $A$  is computed using the visible decay products, which are closely aligned with the original  $\tau$  lepton before decay, especially at high  $p_T$ . In the SR, the events are required to have  $A < 0.015$ . This requirement has a signal efficiency ranging from 95% in the  $e\mu$  final state to  $> 99\%$  in the  $\tau_h\tau_h$  final state.

Elastic signal events are also characterized by a low track multiplicity ( $N_{\text{tracks}}$ ) at the dilepton



vertex. The dilepton vertex position along the  $z$  axis is calculated as the average  $z$  of the two objects. The variable  $N_{\text{tracks}}$  is estimated by counting the number of tracks that have a  $z$  coordinate within a 0.1 cm wide window centered around the dilepton vertex, removing the tracks that were used to build the lepton candidates. The SRs are defined with  $N_{\text{tracks}} = 0$  or 1. About 50 (25)% of the signal events have  $N_{\text{tracks}} = 0$  (1). This fraction is larger far from the beamspot position, where the contribution from PU tracks is less important.

The activity in the tracker impacts the identification of electrons, muons, and  $\tau_h$  candidates, typically leading to a higher efficiency. Scale factors are computed to match the simulated efficiencies to the observed efficiencies for objects surrounded by a low track activity at their vertex, after the standard corrections independent of  $N_{\text{tracks}}$  are applied.

## 6 Corrections to the simulated track multiplicity

The simulations are corrected to describe well  $N_{\text{tracks}}$ , the track multiplicity around the dilepton vertex. Corrections for two sources of tracks are derived: tracks originating from the pileup (Section 6.1) and tracks originating from the hard scattering and underlying event activity (Section 6.2). They are derived from CRs in the dimuon final state and applied to simulations in the SRs.

### 6.1 Tracks originating from the pileup

While the PU multiplicity in simulation is reweighted to match that observed in the data, the PU track density along the  $z$  axis in simulation needs to be corrected to better describe  $N_{\text{tracks}}$  at the dilepton vertex. First, the simulations are corrected such that the beamspot position ( $z_{\text{BS}}$ ) and beamspot width ( $\sigma_{\text{BS}}$ ) distributions are similar to the observed ones, and the PU tracks are redistributed accordingly along the  $z$  axis, as explained below. Simulated events originally all have  $\sigma_{\text{BS}} = 3.5$  cm, whereas the observed  $\sigma_{\text{BS}}$  distribution is spread between about 3.0 and 3.8 cm. Simulated events are assigned randomly corrected beamspot properties,  $z_{\text{BS}}^{\text{corr}}$  and  $\sigma_{\text{BS}}^{\text{corr}}$ , following the corresponding profiles in data. The  $z$  position of PU tracks, identified as such if they are not matched to generator-level information, are redistributed along the  $z$  axis and assigned a corrected  $z$  position:

$$z^{\text{corr}} = z_{\text{BS}}^{\text{corr}} + \frac{\sigma_{\text{BS}}^{\text{corr}}}{\sigma_{\text{BS}}^{\text{sim}}} (z - z_{\text{BS}}^{\text{sim}}). \quad (8)$$

A residual correction to the PU track density is derived in a  $Z \rightarrow \mu\mu$  CR, defined with the selection criteria for the  $\mu\mu$  final state detailed in Section 5, with the additional requirement that  $m_{\mu\mu}$  is within 15 GeV of the true  $Z$  boson mass,  $m_Z$ . The track multiplicity is counted in data and in simulation in windows of 0.1 cm width along the  $z$  axis, for windows centered at least 1 cm away from the reconstructed dimuon vertex, as illustrated in Fig. 2. This last requirement ensures that all tracks in the windows come from PU and not from the hard scattering interaction. Weights are derived as functions of the PU track multiplicity and window  $z$  position so as to match the  $N_{\text{tracks}}$  distribution in data. Distributions of the number of PU tracks,  $N_{\text{tracks}}^{\text{PU}}$ , are shown in data, uncorrected, and beamspot-corrected simulations in Fig. 3, for windows with different  $z$  positions. About one third of the windows situated at the beamspot center do not have any PU track. This fraction reaches about one half (80%) one (two) beamspot widths away from the beamspot center. The correction to the simulated event weight is in the range 0.89–1.00 (0.93–1.16) for  $N_{\text{tracks}}^{\text{PU}} = 0$  ( $N_{\text{tracks}}^{\text{PU}} = 1$ ) over the whole  $z$  axis and data-taking periods.

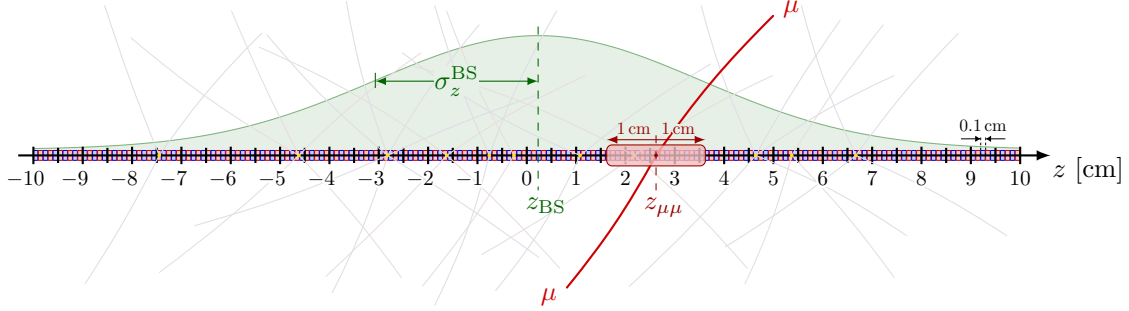


Figure 2: Schematic view of the 0.1 cm-wide windows probed along the  $z$  axis to derive corrections to the PU track density in simulation. Windows within 1 cm from the dimuon vertex, illustrated with the red box, are discarded so as not to count tracks from the hard scattering interaction. The green curve indicates the position and width of the beamspot.

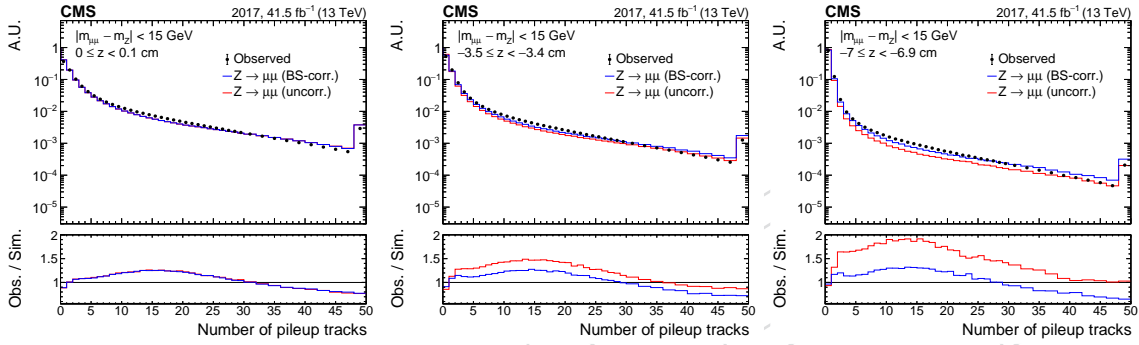


Figure 3: Distribution of  $N_{\text{tracks}}^{\text{PU}}$  in windows of 0.1 cm width along the  $z$  axis in data (black), uncorrected simulation (red), and beamspot-corrected simulation (blue) in data collected in 2017. The windows shown here are located at the beamspot center (left), and one (center) or two (right) beamspot widths away from the center. The ratio of corrected simulation to data is taken as a correction to the simulations.

## 6.2 Tracks originating from the hard scattering and underlying event activity

The only major background in the SR estimated using simulation is the Drell–Yan production of a lepton pair. The number of tracks coming from the hard scattering interaction is not well described in the simulation, and corrections are derived from the same  $Z \rightarrow \mu\mu$  CR. To derive this correction, the number of tracks around the reconstructed dimuon vertex is compared between data and simulation.

As shown in Fig. 4, the simulation is split into several components depending on the number of tracks originating from the hard scattering interaction, as determined from generator-level information, and reconstructed with  $p_T > 0.5 \text{ GeV}$  and  $|\eta| < 2.5$ . The total number of reconstructed tracks is the sum of these tracks and those associated with PU interactions:  $N_{\text{tracks}} = N_{\text{tracks}}^{\text{HS}} + N_{\text{tracks}}^{\text{PU}}$ . Events from the exclusive photon-induced production of a pair of muons or  $W$  bosons, which contribute only significantly at low  $N_{\text{tracks}}$ , are estimated from simulation and subtracted.

The PU track density is first corrected with the weights described in Section 6.1, while the reweighting factors for each Drell–Yan component with a given number of  $N_{\text{tracks}}^{\text{HS}}$  is determined iteratively by matching the simulation to the data, starting from events with  $N_{\text{tracks}} = 0$ , to which only the simulated component with  $N_{\text{tracks}}^{\text{HS}} = 0$  contributes. The event weight correction is as low as  $0.61 \pm 0.04$  ( $0.76 \pm 0.04$ ) for  $N_{\text{tracks}}^{\text{HS}} = 0$  ( $N_{\text{tracks}}^{\text{HS}} = 1$ ). This correction is also applied

to the minor diboson production background with 2 leptons and 2 neutrinos in the final state, which has the same generator settings.

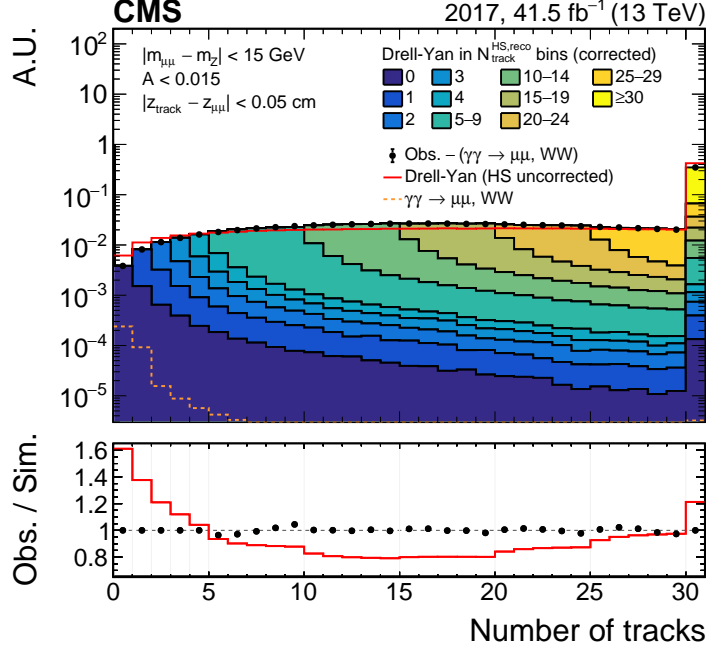


Figure 4: Distribution of the number of reconstructed tracks in a 0.1 cm-wide window in the  $z$  direction, centered on the dimuon reconstructed vertex, for  $A < 0.015$ . The Drell-Yan simulation is split into several components based on the number of reconstructed tracks originating from the hard interaction. The red line shows the simulation before the correction. The expected contribution from the  $\gamma\gamma \rightarrow \mu\mu$  and  $\gamma\gamma \rightarrow WW$  processes (dashed orange line) has been subtracted from observed data. The last bin includes the overflow.

## 7 Signal estimation

The signal is modelled using simulated elastic events. The semi-dissociative and fully dissociative production modes are much less likely to satisfy the acoplanarity and  $N_{\text{tracks}}$  requirement but their cross sections are larger, such that they are not negligible in the SR. The elastic prediction is rescaled to account for the semi-dissociative and fully dissociative contributions as explained in the next paragraph.

The scaling factor is measured in data in a  $\mu\mu$  CR, defined with the baseline selection and  $N_{\text{tracks}} = 0$  or 1 and  $A < 0.015$  as additional requirements. In that CR, shown in Fig. 5, the inclusive backgrounds, dominated by the Drell-Yan production of a muon pair, are estimated together from data. Their  $m_{\mu\mu}$  distribution is taken from observed events with  $3 < N_{\text{tracks}} < 7$ . These thresholds ensure that the photon-induced contributions are negligible while the  $N_{\text{tracks}}$  selection is close enough to that in the SR to have an unbiased  $m_{\mu\mu}$  distribution. The  $m_{\mu\mu}$  distribution is reweighted so that the inclusive background normalization in the range  $|m_{\mu\mu} - m_Z| < 15 \text{ GeV}$  matches the data count in the same range. The elastic  $\gamma\gamma \rightarrow \mu\mu$  process is then rescaled to match the difference between the data and the inclusive backgrounds away from the Z peak region.

Assuming there is no dependence on the dilepton mass,  $m_{\ell\ell}$ , the scaling factor to include the dissociative contributions is  $2.70 \pm 0.04$  ( $2.71 \pm 0.10$ ) for  $N_{\text{tracks}} = 0$  (1), where the uncertainty is statistical only. This is compatible with the value predicted by the SUPERCHIC generator, using

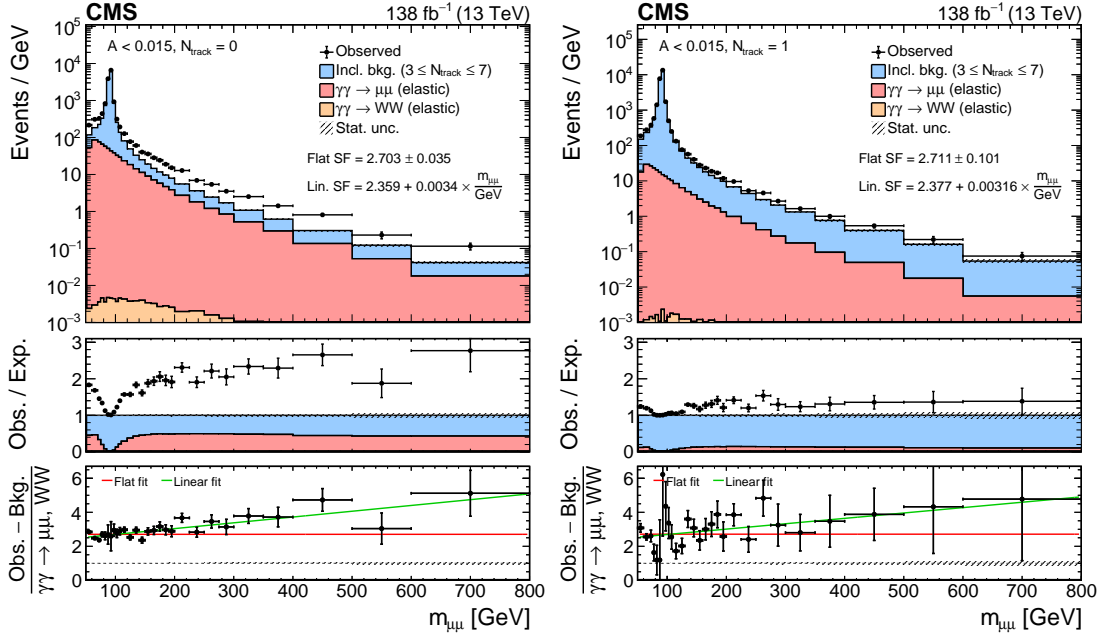


Figure 5: Measurement of the scaling factor for the elastic-elastic exclusive signal in  $\mu\mu$  events for  $N_{\text{tracks}} = 0$  (left) or 1 (right), and  $A < 0.015$ . The shape of the inclusive background (blue) is estimated from the observed data in the  $3 \leq N_{\text{tracks}} \leq 7$  sideband, and rescaled to fit the observed data in  $75 < m_{\mu\mu} < 105$  GeV. The scaling factor is fitted in the bottom ratio pad with constant (red) and linear (green) functions.

the same acoplanarity requirement  $A < 0.015$ . The scaling factor is also fitted as a linear function of  $m_{\mu\mu}$  and, in that case, is equal to  $2.359 + 0.0034 m_{\mu\mu} / \text{GeV}$  ( $2.377 + 0.00316 m_{\mu\mu} / \text{GeV}$ ) for  $N_{\text{tracks}} = 0$  (1). A linear dependency of the scaling factor with  $m_{\ell\ell}$  is assumed as a nominal correction in the SRs, whereas the flat value is considered as a systematic uncertainty as detailed in Section 9. Elastic events in the SR, coming from the  $\gamma\gamma \rightarrow \tau\tau/ee/\mu\mu/WW$  simulations, are all rescaled with this correction as a function of the dilepton or diboson mass, to include semi-dissociative and fully-dissociative contributions.

## 8 Background estimation

In the SR, the dominant backgrounds are the Drell–Yan production of a lepton pair and processes with a jet misidentified as an electron, a muon, or a  $\tau_h$  candidate, collectively denoted as “jet mis-ID background”. The jet mis-ID background is essentially composed of  $W$  + jets and QCD multijet events. The photon-induced production of a pair of  $W$  bosons is reduced with the acoplanarity requirement, and is significant only in the  $e\mu$  final state, where its expected normalization is about 4% of that of the exclusive di- $\tau$  production. The photon-induced production of an electron (muon) pair is about 50 (4)% of the signal expected contribution in the  $e\tau_h$  ( $\mu\tau_h$ ) final state. When there is no exclusivity requirement relying on  $A$  nor  $N_{\text{tracks}}$ , the  $t\bar{t}$ , inclusive diboson, and single-top-quark processes also contribute.

### 8.1 Drell–Yan

The Drell–Yan process is estimated using simulation. The corrections described in Section 6 are applied to improve the description of  $N_{\text{tracks}}^{\text{PU}}$  and  $N_{\text{tracks}}^{\text{HS}}$ . The acoplanarity is observed to be mismodeled in simulation in a  $\mu\mu$  CR, defined with the selection criteria from Section 5 and further enriched in Drell–Yan events by requiring  $|m_{\mu\mu} - m_Z| < 15$  GeV. An acoplanarity

correction, measured in two-dimensional bins of the  $p_T$  of both muons, is derived in this CR by matching the simulation to the observed data. This correction is applied to simulated Drell–Yan events in the SR on the basis of the generated  $\tau$  lepton  $p_T$  before their decays.

The simulation size is limited, and large statistical uncertainties arise when requiring  $N_{\text{tracks}} = 0$  or 1. To reduce this effect, the Drell–Yan contribution in the SR is estimated from simulated events with  $N_{\text{tracks}} < 10$ , which constitute about 10% of the total number of Drell–Yan events. The upper bound ensures a similar event topology as in the SR, allowing the  $m_{\tau\tau}$  distributions to be similar. The distribution derived with  $N_{\text{tracks}} < 10$  is scaled to predict the Drell–Yan events with  $N_{\text{tracks}} = 0$  or 1. The scaling factors are derived in the  $e\mu$  final state with a large simulation of  $Z \rightarrow \tau\tau$  events with only leptonic  $\tau$  decays. They are equal to  $2.48 \pm 0.05\%$  and  $5.10 \pm 0.07\%$ , for  $N_{\text{tracks}} = 0$  and 1, respectively.

## 8.2 Backgrounds with misidentified jets in the $e\tau_h$ and $\mu\tau_h$ final states

The mis-ID background with a jet misidentified as a  $\tau_h$  candidate is estimated from data. In the  $e\tau_h$  and  $\mu\tau_h$  final states, the dominant processes contributing to the mis-ID background are  $W + \text{jets}$  and QCD multijet events. The jet misidentification factors (MFs) depend on the process because of different topologies and jet flavors, and they are therefore measured in two different CRs. A CR enriched in  $W + \text{jets}$  events is built by requiring  $m_T > 75 \text{ GeV}$ , while a QCD-enriched CR is obtained by requiring the two objects to have same-sign (SS) charge. In these CRs, the MFs are measured for each data-taking period, separately for each  $\tau_h$  DM, by taking the ratio of events in which the  $\tau_h$  candidate passes the SR  $\tau_h$  identification criteria, to events in which the  $\tau_h$  candidate fails these criteria but passes looser ones. Events where the  $\tau_h$  candidate is genuine or corresponds to a misidentified electron or muon are evaluated using simulation and subtracted from the CR. The MFs are fitted as a function of the  $\tau_h$   $p_T$  and range from about 0.03 for the  $h^\pm h^\mp h^\pm + \pi^0(\text{s})$  DM, to about 0.40 for the  $h^\pm$  DM. These MFs are multiplied by a factor of about 1.7 when the events are selected with cross-triggers relying on the presence of a  $\tau_h$  candidate because of the isolation cuts applied at trigger level.

The track activity around the di- $\tau$  impacts the calculation of the  $\tau_h$  isolation, which enters the  $\tau_h$  identification discriminator, such that the MFs are expected to depend on  $N_{\text{tracks}}$ . For each  $\tau_h$  DM, the MFs determined for given ranges of  $N_{\text{tracks}}$  are divided by the average MF measured inclusively in  $N_{\text{tracks}}$  to obtain a multiplicative  $N_{\text{tracks}}$ -dependent correction,  $\omega(N_{\text{tracks}}, \text{DM}^{\tau_h})$ , to the  $p_T$ - and decay-mode-dependent MFs determined previously. The corrected MFs can then be written, for each CR, as:

$$\text{MF}^{\text{corr}}(p_T^{\tau_h}, \text{DM}^{\tau_h}, N_{\text{tracks}}) = \text{MF}(p_T^{\tau_h}, \text{DM}^{\tau_h}) \omega(N_{\text{tracks}}, \text{DM}^{\tau_h}). \quad (9)$$

The  $\omega(N_{\text{tracks}}, \text{DM}^{\tau_h})$  corrections are measured for the combination of the different data-taking years. Because statistical uncertainties are large at low  $N_{\text{tracks}}$ ,  $\omega(N_{\text{tracks}}, \text{DM}^{\tau_h})$  is fitted with an exponential function for  $N_{\text{tracks}} < 10$ –15, as shown in Fig. 6 for the  $h^\pm + \pi^0(\text{s})$  DM in the  $e\tau_h$  final state.

The total MF,  $\text{MF}_{\text{tot}}$ , is computed as a weighted average of the MFs determined in the high- $m_T$  and SS CRs, according to the expected relative fraction of  $W + \text{jets}$  and QCD multijet events:

$$\text{MF}_{\text{tot}} = x^{\text{QCD}} \text{MF}_{\text{SS}}^{\text{corr}} + (1 - x^{\text{QCD}}) \text{MF}_{\text{high-}m_T}^{\text{corr}}, \quad (10)$$

where  $x^{\text{QCD}} = N^{\text{QCD}} / (N^{\text{QCD}} + N^W)$ . The number of  $W + \text{jets}$  events passing the baseline selection,  $N^W$ , is determined from simulations, while the same quantity for QCD multijet events,  $N^{\text{QCD}}$ , is taken as the difference between data and simulated predictions for other processes in the SS CR.



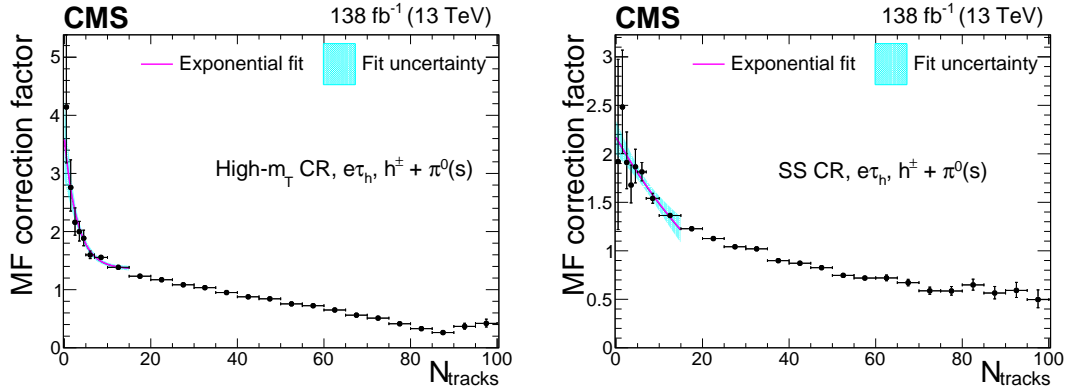


Figure 6: Multiplicative  $N_{\text{tracks}}$ -dependent corrections to the  $\tau_h$  MFs,  $\omega(N_{\text{tracks}}, \text{DM}_h^\tau)$ , in the  $e\tau_h$  final state, in the high- $m_T$  (left) and SS (right) CRs, for the  $h^\pm + \pi^0(s)$  DM. The cyan shaded area corresponds to the fit uncertainty.

To estimate the mis-ID background in the SR in the  $e\tau_h$  and  $\mu\tau_h$  final states, events passing the SR selection with the exception that the  $\tau_h$  candidate fails the  $\tau_h$  nominal identification but passes looser criteria, are reweighted with  $\text{MF}_{\text{tot}}$ . Contributions from events with real  $\tau_h$ , electrons, or muons are estimated from simulation and subtracted from the anti-isolated region.

### 8.3 Backgrounds with misidentified jets in the $\tau_h\tau_h$ final state

In the  $\tau_h\tau_h$  final state, the mis-ID background is mostly composed of QCD multijet events and the MFs are determined in a single CR where the  $\tau_h$  candidates have SS charge. The MFs for the leading (subleading)  $\tau_h$  are measured in events in which the subleading (leading)  $\tau_h$  passes or fails the tight identification criteria. They are in the range 0.05–0.38 depending on the  $\tau_h$  DM.

The  $N_{\text{tracks}}$ -dependent correction is derived in a similar way as in the  $e\tau_h$  and  $\mu\tau_h$  final states, and is between 1.8 and 2.3 for events with  $N_{\text{tracks}} = 0$ . In this final state, the number of events selected at low  $N_{\text{tracks}}$  is larger because of the inversion of the isolation of both  $\tau_h$  candidates, and contributions from exclusive dijet production become significant in the lowest  $N_{\text{tracks}}$  bins, such that no fit is performed to the  $\omega(N_{\text{tracks}}, \text{DM}_h^\tau)$  distributions, and the values measured for  $N_{\text{tracks}} = 0, 1$  are used without constraints from higher  $N_{\text{tracks}}$  bins.

In the SR, events where the leading (subleading)  $\tau_h$  is a misidentified jet are estimated by scaling with the MFs events where the leading (subleading)  $\tau_h$  is anti-isolated and the subleading (leading)  $\tau_h$  is isolated. These contributions both include events where both the leading and subleading  $\tau_h$  candidates are misidentified jets. To remove the double counting, events with two misidentified jets are estimated by scaling events where the two  $\tau_h$  candidates are anti-isolated with the product of the MFs for each object, and are subtracted.

### 8.4 Backgrounds with misidentified jets in the $e\mu$ final state

In the  $e\mu$  final state, the mis-ID background with a jet misidentified as an electron or a muon, essentially composed of  $W + \text{jets}$  and QCD multijet events, is estimated from events where the electron and muon have SS charge. Events passing the SR selection with the exception that the electron and muon have SS charge are reweighted with a two-dimensional scaling factor dependent on the electron and muon  $p_T$ . This factor is measured by taking the ratio of OS to SS events where the muon isolation is inverted, subtracting non-jet contributions estimated from simulation. It is in the range 1.4–2.1 depending on the lepton  $p_T$ .

A bias is introduced by the inversion of the muon isolation, and a correction to the scaling factor



is measured by taking the ratio of the scaling factors measured in events where the electron identification is inverted, and the muon isolation is inverted or not. The correction ranges between 1.0 and 2.7 depending on the lepton  $p_T$ .

A multiplicative correction for the dependency of the scaling factor with  $N_{\text{tracks}}$  is measured by fitting the ratio of the scaling factors in exclusive ranges of  $N_{\text{tracks}}$  over the average inclusive scaling factor. At  $N_{\text{tracks}} = 0$ , the correction is about  $0.89 \pm 0.07$ .

While the normalization of the jet mis-ID background is estimated with the procedure described above, its  $m_{\text{vis}}$  distribution is taken from SS data events with  $N_{\text{tracks}} < 10$ , from which backgrounds other than the jet mis-ID component are subtracted using their simulated expectations. This method reduces statistical fluctuations in the  $m_{\text{vis}}$  templates.

### 8.5 Other backgrounds

Minor contributions from diboson events to the SR, mostly WW events, are estimated from simulation. The exclusive  $\gamma\gamma \rightarrow WW$ ,  $\gamma\gamma \rightarrow ee$ , and  $\gamma\gamma \rightarrow \mu\mu$  events, which contribute mostly to the  $e\mu$ ,  $e\tau_h$ , and  $\mu\tau_h$  final states, respectively, are estimated from the elastic simulation and rescaled with the same correction as the signal samples to include the dissociative components.

The agreement between data and predictions is checked in events passing the selection without the  $N_{\text{tracks}}$  and acoplanarity requirements. The single-top quark,  $t\bar{t}$ , and Higgs boson processes, which do not contribute to the SR with  $N_{\text{tracks}} < 2$ , are included using their prediction from simulation. The agreement is good for all final states.

## 9 Systematic uncertainties

Systematic uncertainties are considered as nuisance parameters in the statistical procedure to extract the signal significance, its signal strength  $\mu$ , and constraints on  $a_\tau$  and  $d_\tau$ . The signal strength  $\mu$  is defined as the ratio between the observed cross section of the  $\gamma\gamma \rightarrow \tau\tau$  process to the theoretical cross section predicted by the GAMMA-UPC generator for the elastic component corrected by the multiplicative experimental scaling to include dissociative contributions.

The integrated luminosities for the 2016, 2017, and 2018 data-taking years have 1.2–2.5% individual uncertainties [56–58], while the overall uncertainty for the 2016–2018 period is 1.6%. The uncertainty in the Drell–Yan theoretical cross section is 2%.

The uncertainties in the muon and electron identification, isolation, and triggering efficiencies are up to 2% per object. Uncertainties related to the  $\tau_h$  trigger efficiency depend on  $DM^{\tau_h}$  and are up to 5%. Several uncertainties, stemming from statistical and systematic sources in the measurement, affect the  $\tau_h$  identification, with different correlations across data-taking years and various dependencies on the  $\tau_h$  DM and its  $p_T$ . This uncertainty is up to 5% in the  $p_T$  range considered in this analysis, and propagates directly to the measured signal strength. Electrons (muons) misidentified as  $\tau_h$  candidates, coming mostly from the  $Z \rightarrow ee$  ( $Z \rightarrow \mu\mu$ ) process, have normalization uncertainties of the order of 10 (10)%. The uncertainty in the  $\tau_h$  energy scale is up to 1.2%, whereas electrons (muons) misidentified as  $\tau_h$  have energy scale uncertainties up to 5 (1)%. Multiplicative corrections to the scale factors to account for the low  $N_{\text{tracks}}$  environment have uncertainties of 2.1, 2.0, 15, and 22% for genuine  $\tau_h$  candidates, electrons, muons misidentified as  $\tau_h$  candidates, and electrons misidentified as  $\tau_h$  candidates, respectively.

The uncertainty in the  $N_{\text{tracks}}^{\text{PU}}$  correction amounts to 2%, which covers the effects of the beamspot

width and position correction. The uncertainty in the  $N_{\text{tracks}}^{\text{HS}}$  correction is taken to have the same magnitude as the relative fraction of  $\gamma\gamma \rightarrow \mu\mu/\text{WW}$  events in the CR where the correction is derived, and it amounts to 6.5 (1.5)% in the  $N_{\text{tracks}} = 0(1)$  category. The statistical uncertainty in the correction is negligible with respect to this systematic component. This uncertainty contributes a 7% effect in the measured signal strength as shown in Fig. 7 (second line) and is among the leading systematic uncertainties in this analysis.

The correction to the acoplanarity distribution in simulated Drell–Yan events leads to a 5% normalization uncertainty, arising from the finite granularity used to bin the correction as a function of the  $p_T$  of the two leptons. An uncertainty of 2.0 (1.4)% is associated with the estimation of the Drell–Yan events in the SR with  $N_{\text{tracks}} = 0(1)$  from simulated events with  $N_{\text{tracks}} < 10$ . Uncertainties arising from the renormalization and factorization scales, as well as from the PDF set, are also taken into account for the Drell–Yan simulation, after propagation to the acoplanarity correction.

The uncertainty in the predictions of the jet mis-ID background in final states with  $\tau_h$  candidates comes from several sources:

- A statistical uncertainty in the inclusive MFs, growing linearly to 50% for  $p_T^{\tau_h} = 300$  GeV, independently for each DM and data-taking year;
- A statistical uncertainty in the  $N_{\text{tracks}}$  correction, amounting to 18 (16, 6)% in the  $e\tau_h$  ( $\mu\tau_h, \tau_h\tau_h$ ) SRs;
- A systematic uncertainty in the inclusive MFs, coming from the inversion of selection requirements to define the CRs, reaching up to 10%;
- A systematic uncertainty in the calculation of the relative fraction of  $W + \text{jets}$  and QCD multijet events in the  $e\tau_h$  and  $\mu\tau_h$  SRs, leading to a 9% normalization effect;
- A systematic uncertainty in the  $N_{\text{tracks}}$  correction, arising from the choice of the fit function and fit range, with an effect up to 10% for  $N_{\text{tracks}} = 0$ .

Statistical uncertainties in the OS-to-SS scaling factor used to evaluate the mis-ID background in the  $e\mu$  final state are included, independently for each bin in electron and muon  $p_T$  where the measurement is performed. A systematic uncertainty of 10% is considered on top to cover for a potential difference in the background composition in the SR and CR. The extrapolation of the scaling factor to  $N_{\text{tracks}} = 0$  has a total uncertainty of 8%, arising from the choice of the fit function and from the limited number of events in the measurement.

Most theoretical and experimental uncertainties cancel when renormalizing the signal prediction using the scaling factor derived from the  $\mu\mu$  CR for the  $\gamma\gamma \rightarrow \mu\mu$  process. The uncertainty in the scaling factor is composed of a normalization component from statistical origin, amounting to 1.3 (3.7)% for  $N_{\text{tracks}} = 0(1)$ , and a component with a shape dependence on  $m_{\tau\tau}$ . The latter component consists in considering as a 1 s.d. effect the possibility that the scaling factor does not depend on  $m_{\ell\ell}$ , and is symmetrized with respect to the nominal hypothesis of a linear dependence with  $m_{\ell\ell}$ . This  $m_{\tau\tau}$ -dependent uncertainty is the leading uncertainty in the measurement of the  $\gamma\gamma \rightarrow \tau\tau$  process, as shown in Fig. 7 (first line), and contributes a 16% uncertainty to the measured signal strength. These uncertainties are also considered for the photon-induced WW, ee, and  $\mu\mu$  productions.

Statistical uncertainties in the number of simulated background events in the SR or observed event yields in the CRs used to derive the jet mis-ID background are considered in all bins of the distributions using the approach from Ref. [59]. The systematic uncertainty in the pileup modelling is taken into account by varying by  $\pm 4.6\%$  the total inelastic cross section used to

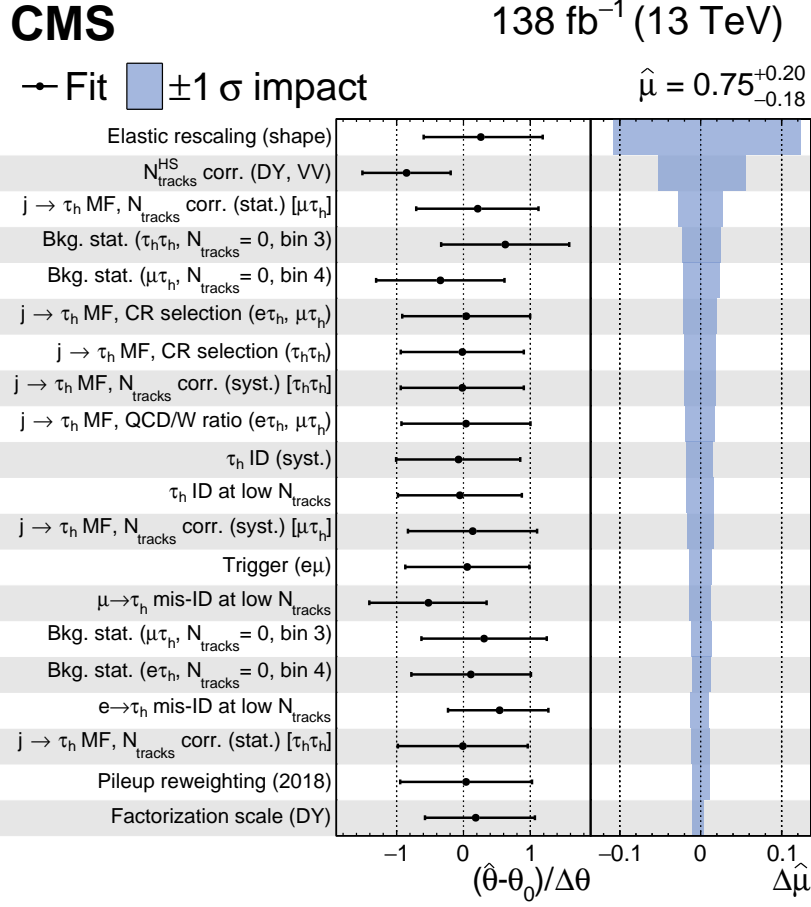


Figure 7: Postfit values of the nuisance parameters (black markers), shown as the difference of their best-fit values,  $\hat{\theta}$ , and prefit values,  $\theta_0$ , relative to the prefit uncertainties  $\Delta\theta$ . The impact  $\Delta\hat{\mu}$  of the nuisance parameters on the signal strength is computed as the difference of the nominal best fit value of  $\mu$  and the best fit value obtained when fixing the nuisance parameter under scrutiny to its best fit value  $\hat{\theta}$  plus/minus its postfit uncertainty (blue shaded area). The nuisance parameters are ordered by their impact, and only the 20 highest ranked parameters are shown.

499 calculate simulated pileup distributions [60].

500 The impacts of the leading systematic uncertainties in the measurement of the signal strength,  
 501 which is described in Section 10.1, are shown in Fig. 7.

## 502 10 Results

503 The significance of the photon-induced  $\gamma\gamma \rightarrow \tau\tau$  process, as well as the constraints on  $a_\tau$  and  
 504  $d_\tau$ , are extracted from the  $m_{\text{vis}}$  distributions in the four final states and in the two  $N_{\text{tracks}}$  bins,  
 505 shown in Figs. 8–9. The last bins include events up to  $m_{\text{vis}} = 500$  GeV, while events at higher  
 506  $m_{\text{vis}}$  are discarded to ensure a sufficient difference with the  $\Lambda$  scale used in the BSM interpre-  
 507 tation. This upper threshold removes SM signal events at the percent level. The systematic  
 508 uncertainties described in Section 9 are included in the statistical procedure as The number of  
 509 data events in the  $N_{\text{tracks}} = 0$  SRs, with the additional requirement that  $m_{\text{vis}}$  is greater than  
 510 100 GeV to reduce the Drell–Yan background contribution, is compared in Table 2 to the back-

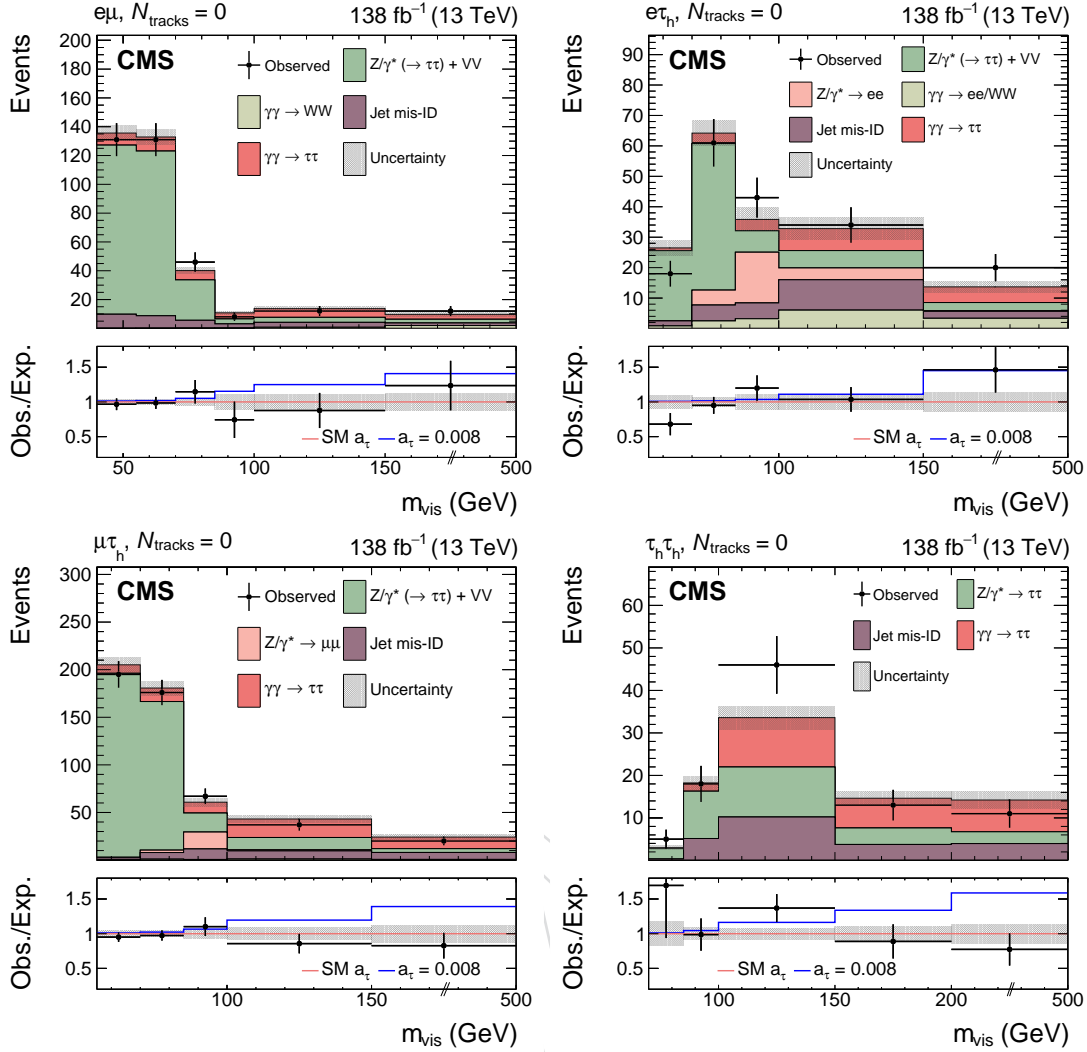


Figure 8: Observed and predicted  $m_{\text{vis}}$  distributions in the  $e\mu$  (upper left),  $e\tau_h$  (upper right),  $\mu\tau_h$  (lower left), and  $\tau_h\tau_h$  (lower right) final states for events with  $N_{\text{tracks}} = 0$ . The minor inclusive diboson background contribution is drawn together with the Drell–Yan background in the  $e\mu$ ,  $e\tau_h$ , and  $\mu\tau_h$  final states. The normalization of the predicted background distributions corresponds to the result of the global fit. The signal distribution is normalized to its best fit signal strength. The uncertainty band accounts for all sources of background and signal uncertainty, systematic as well as statistical, after the global fit. In the fit,  $a_\tau$  and  $d_\tau$  are fixed to their SM values. The ratio of the total predictions for an illustrative value of  $a_\tau = 0.008$  to the those with SM electromagnetic couplings is shown with a blue line in the bottom panel.

ground and signal yields in the different final states. nuisance parameters.

## 10.1 Observation of $\gamma\gamma \rightarrow \tau\tau$

The observed (expected) significance is 5.3 (6.5) s.d. for the exclusive  $\gamma\gamma \rightarrow \tau\tau$  process. This constitutes the first observation of this process in pp collisions. The corresponding significances per final state are 2.3, 3.0, 2.1, and 3.4 (3.2, 2.1, 3.9, and 3.9) s.d. in the  $e\mu$ ,  $e\tau_h$ ,  $\mu\tau_h$ , and  $\tau_h\tau_h$  final states, respectively. The most sensitive channel in terms of expected significance is  $\mu\tau_h$  because of its larger branching fraction with respect to the  $e\mu$  final state, its lower  $p_T$  thresholds and higher lepton efficiencies with respect to the  $e\tau_h$  final state, and its lower background

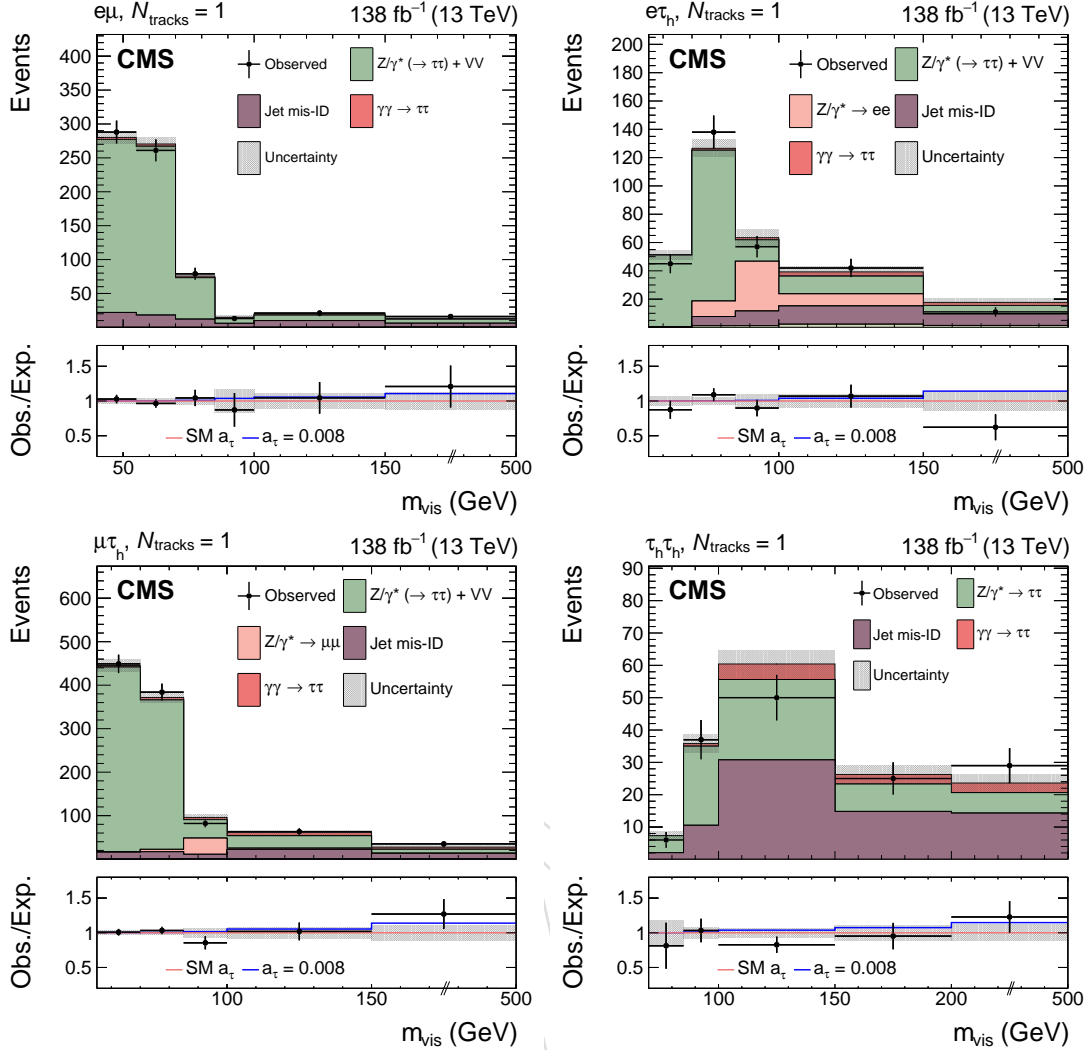


Figure 9: Observed and predicted  $m_{\text{vis}}$  distributions in the  $e\mu$  (upper left),  $e\tau_h$  (upper right),  $\mu\tau_h$  (lower left), and  $\tau_h\tau_h$  (lower right) final states for events with  $N_{\text{tracks}} = 1$ . The description of the histograms is the same as in Fig. 8.

Table 2: Observed and predicted event yields per final state in the signal-enriched phase space with  $m_{\text{vis}} > 100 \text{ GeV}$  and  $N_{\text{tracks}} = 0$ . The signal and background yields are the result of the global fit including all sources of uncertainties.

Process	$e\mu$	$e\tau_h$	$\mu\tau_h$	$\tau_h\tau_h$
$Z/\gamma^* \rightarrow \tau\tau$	$3.6 \pm 0.5$	$9.0 \pm 1.2$	$18.7 \pm 2.9$	$20.2 \pm 3.1$
$Z/\gamma^* \rightarrow ee/\mu\mu$	—	$3.9 \pm 1.2$	$1.6 \pm 0.6$	—
Jet mis-ID	$5.0 \pm 0.8$	$11.4 \pm 2.9$	$16.5 \pm 3.6$	$17.5 \pm 2.8$
Inclusive VV	$3.0 \pm 0.3$	$0.2 \pm 0.0$	$0.4 \pm 0.0$	—
$\gamma\gamma \rightarrow ee/\mu\mu$	—	$8.1 \pm 2.3$	$1.4 \pm 0.2$	—
$\gamma\gamma \rightarrow WW$	$2.5 \pm 0.6$	$0.1 \pm 0.0$	$0.4 \pm 0.1$	—
Total bkg.	$14.1 \pm 1.3$	$32.8 \pm 4.8$	$38.9 \pm 4.4$	$37.7 \pm 4.2$
Signal	$11.9 \pm 4.2$	$15.8 \pm 5.7$	$40.3 \pm 14.2$	$33.4 \pm 11.2$
Total	$26.0 \pm 3.8$	$48.5 \pm 4.7$	$79.2 \pm 13.6$	$71.1 \pm 9.3$
Observed	24	54	57	70

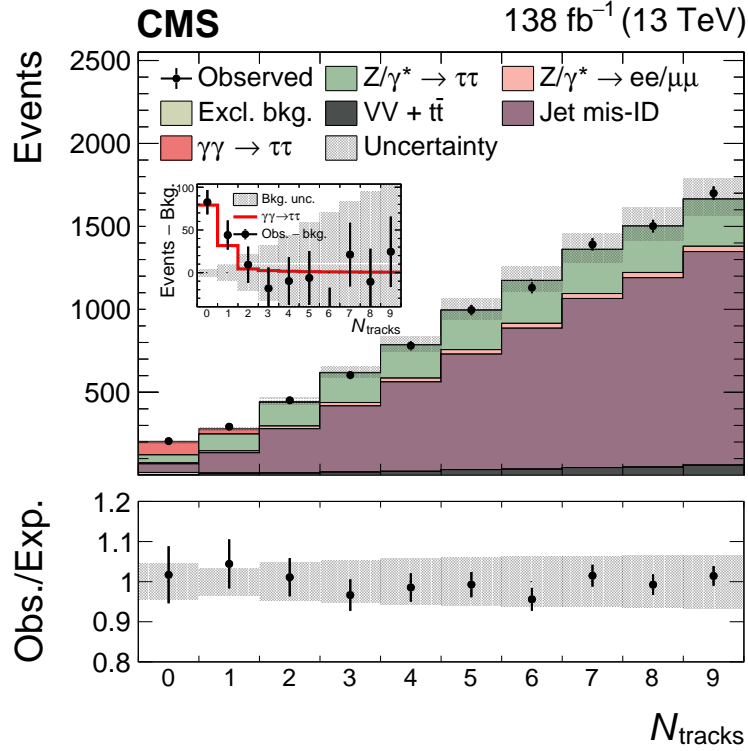


Figure 10: Observed and predicted  $N_{\text{tracks}}$  distributions for events passing the SR selection but with the relaxed requirement  $N_{\text{tracks}} < 10$  and the additional requirement  $m_{\text{vis}} > 100$  GeV, combining the  $e\mu$ ,  $e\tau_h$ ,  $\mu\tau_h$ , and  $\tau_h\tau_h$  final states together. The inclusive diboson background contribution is drawn together with the  $t\bar{t}$  process. The predicted distributions are adjusted to the result of the global fit performed with the  $m_{\text{vis}}$  distributions in the SRs, and the signal distribution is normalized to its best fit signal strength. The inset shows the difference between the observed events and the backgrounds, as well as the signal contribution. Systematic uncertainties are assumed to be uncorrelated between final states to draw the uncertainty band.

contributions with respect to the  $\tau_h\tau_h$  final state.

The  $N_{\text{tracks}}$  distribution for events with  $N_{\text{tracks}} < 10$  is shown for the combination of final states in Fig. 10 for events with  $A < 0.015$ , as in the SR, and  $m_{\text{vis}} > 100$  GeV, so as to reduce the Drell–Yan background contribution. The signal contribution is visible as an excess of events over the inclusive background in the first bins, while the agreement between prediction and observation in the other bins demonstrates a good control of the background modelling and more specifically of the  $N_{\text{tracks}}$  corrections to the simulations and to the MFs used to predict the background with misidentified jets.

We measure a best-fit signal strength of  $\hat{\mu} = 0.75^{+0.21}_{-0.18}$ , where the systematic uncertainty dominates over the statistical uncertainty ( $\hat{\mu} = 0.75^{+0.17}_{-0.14}(\text{syst}) \pm 0.11(\text{stat})$ ). Using only the SRs with  $N_{\text{tracks}} = 0$  and discarding the SRs with  $N_{\text{tracks}} = 1$ , the signal strength becomes  $\hat{\mu}(N_{\text{tracks}} = 0) = 0.69^{+0.23}_{-0.19}$ . The later measurement is used in the determination of the fiducial cross section.

The cross section of the  $\gamma\gamma \rightarrow \tau\tau$  process is measured in a fiducial phase space defined to be as close as possible to the reconstructed event selection. All variables used in the definition of the fiducial region are calculated at the generator level after parton showering and hadronization, and the electrons and muons are “dressed” in that the lepton momentum includes the momenta



of photons radiated within a cone of  $\Delta R < 0.1$  centered on the lepton. The visible  $\tau$  decay products at the generator level are required to have an acoplanarity  $A < 0.015$  and an invariant mass less than 500 GeV. The term visible refers to the kinematic variables constructed from the momenta of the visible decay products of the  $\tau$  leptons, excluding the invisible neutrinos. The di- $\tau$  invariant mass, including the neutrinos, is required to be greater than 50 GeV. There must not be any charged particle with  $p_T > 0.5$  GeV and  $|\eta| < 2.5$  outside of the  $\tau$  lepton decay products. The other requirements depend on the final state. In the  $e\mu$  final state, the leading dressed lepton must satisfy  $p_T > 24$  GeV while the requirement for the subleading lepton is  $p_T > 15$  GeV. The electron (muon) must have  $|\eta| < 2.5$  (2.4). In the  $e\tau_h$  ( $\mu\tau_h$ ) final state, the electron (muon) is required to have  $p_T > 25$  GeV and  $|\eta| < 2.5$  ( $p_T > 21$  GeV and  $|\eta| < 2.4$ ), while the visible  $\tau_h$  must have  $p_T > 30$  GeV and  $|\eta| < 2.3$ . In addition, the transverse mass  $m_T(e/\mu, \vec{p}_T^{\text{miss}})$  must be less than 75 GeV. In the  $\tau_h\tau_h$  final state, both visible  $\tau_h$  at the generator level must have  $p_T > 40$  GeV and  $|\eta| < 2.3$ . Other di- $\tau$  decay modes are considered to be outside of the fiducial region. Using the SRs with  $N_{\text{tracks}} = 0$ , the fiducial cross section is measured to be  $\sigma_{\text{obs}}^{\text{fid}} = 11.2^{+3.1}_{-2.4} (\text{syst})^{+2.2}_{-2.1} (\text{stat})$  fb. This can be compared to the prediction from the GAMMA-UPC generator for the elastic component of the signal, rescaled by our data-driven correction to include dissociative contributions:  $\sigma_{\text{pred}}^{\text{fid}} = 16.5 \pm 1.5$  fb, where the uncertainty is dominated by the uncertainty in the data-driven correction.

## 10.2 Constraints on the anomalous electromagnetic moments of the $\tau$ lepton

Constraints on  $a_\tau$  and  $d_\tau$  are set independently by performing a negative log-likelihood scan with  $a_\tau$  and  $d_\tau$  as single parameters of interest. The SM normalization of  $\gamma\gamma \rightarrow \tau\tau$  is constrained to its predicted value [27], estimated from the elastic simulation and weighted with the scaling factor from the  $\mu\mu$  CR to include dissociative contributions. Varying  $a_\tau$  and  $d_\tau$  from their SM values modifies both the normalization of the signal process and its  $m_{\text{vis}}$  distribution. In particular, the number of predicted signal events increases with  $m_{\text{vis}}$  for large  $|a_\tau|$  values, as shown in the ratio panels of Figs. 8–9 for an illustrative value of  $a_\tau = 0.008$ .

The combination of all final states and years gives an observed (expected) best-fit value of  $a_\tau = 0.0009^{+0.0032}_{-0.0031}$  ( $0.0012^{+0.0041}_{-0.0043}$ ) at 68% confidence level (CL), as shown in Fig. 11 (left). Contrary to the signal strength measurement assuming SM values for  $a_\tau$  and  $d_\tau$ , the statistical uncertainty dominates in the measurement of  $a_\tau$  because the sensitivity is driven by the high- $m_{\text{vis}}$  bins where BSM effects are enhanced:  $a_\tau = 0.0009^{+0.0016}_{-0.0015} (\text{syst})^{+0.0028}_{-0.0027} (\text{stat})$ . If the measurement was performed using only information about the  $m_{\text{vis}}$  distribution and with a floating normalization for the  $\gamma\gamma \rightarrow \tau\tau$  process, the expected precision in the measurement of  $a_\tau$  would decrease by about 50%. The corresponding constraint at 95% CL is:  $-0.0042 < a_\tau < 0.0062$  ( $-0.0051 < a_\tau < 0.0072$ ). The 68% CL constraint on  $d_\tau$  is  $-1.7 < d_\tau < 1.7 \times 10^{-17} e\text{cm}$  ( $-2.3 < d_\tau < 2.3 \times 10^{-17} e\text{cm}$ ), while the 95% CL interval is  $-2.9 < d_\tau < 2.9 \times 10^{-17} e\text{cm}$  ( $-3.4 < d_\tau < 3.4 \times 10^{-17} e\text{cm}$ ). These results are compared to constraints from other experiments in Fig. 12.

The constraints on  $a_\tau$  and  $d_\tau$  can be converted to two-dimensional constraints on the real and imaginary parts of the Wilson coefficients  $C_{\tau B}$  and  $C_{\tau W}$  divided by  $\Lambda^2$ , using Eq. (5). The 95% CL intervals in the plane of the normalized Wilson coefficients are shown in Fig. 13.

## 11 Summary

The exclusive photon-induced production of a pair of  $\tau$  leptons,  $\gamma\gamma \rightarrow \tau\tau$ , has been observed for the first time in proton-proton collisions, with a significance of 5.3 standard deviations (6.5 standard deviations expected). The signal was separated from the inclusive background pro-

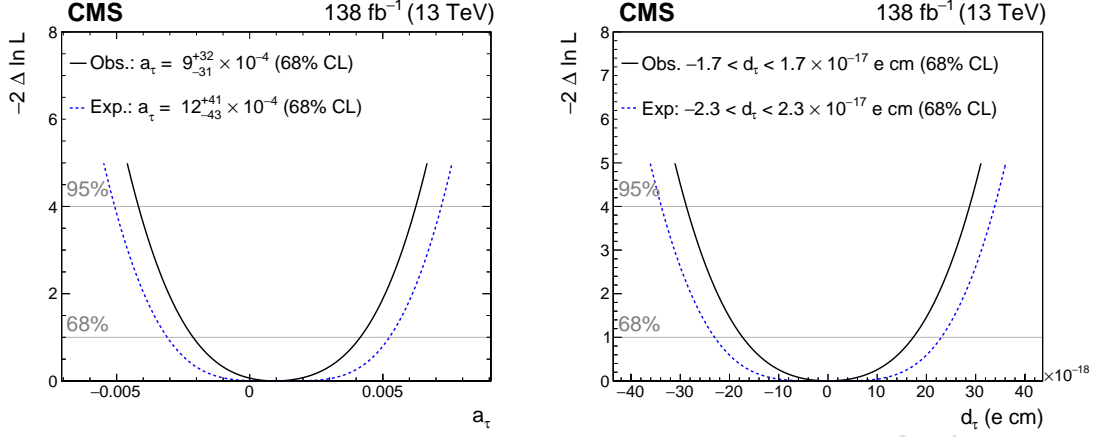


Figure 11: Expected and observed negative log-likelihood scans as a function of  $a_\tau$  (left) and  $d_\tau$  (right), for the combination of all SRs in all data-taking periods.

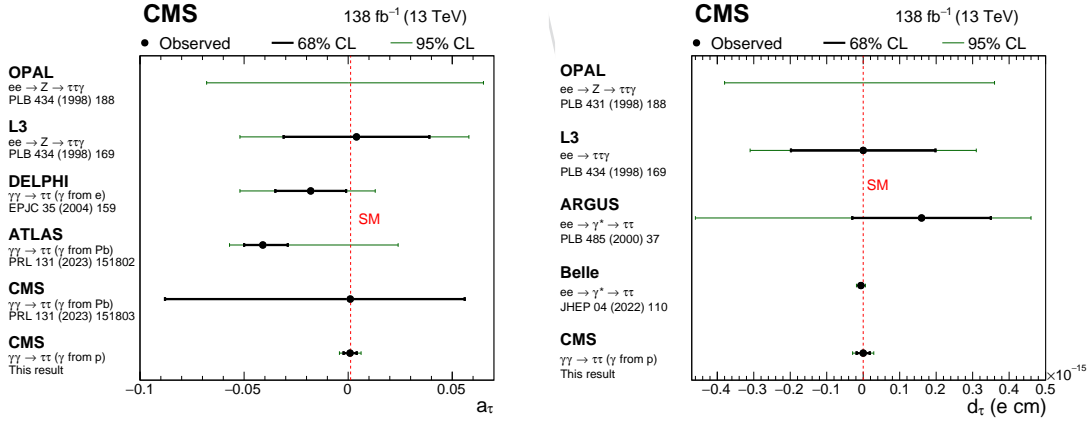


Figure 12: Measurements of  $a_\tau$  (left) and  $d_\tau$  (right) performed in this analysis, compared with previous results from the OPAL, L3, ARGUS, Belle, CMS, and ATLAS experiments [12, 13, 15–18]. Confidence intervals at 68 and 95% CL are shown with thick black and thin green lines, respectively.

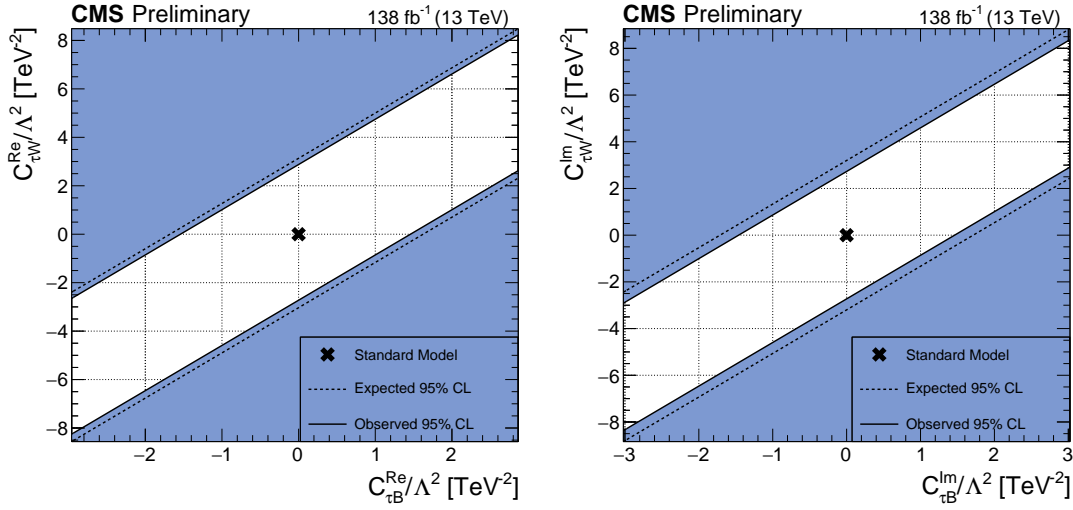


Figure 13: Expected and observed 95% CL constraints on the real (left) and imaginary (right) parts of the Wilson coefficients  $C_{\tau B}$  and  $C_{\tau W}$  divided by  $\Lambda^2$ . The SM value is indicated with a cross.

cesses by requiring a low track activity around the di- $\tau$  vertex and a low acoplanarity between the  $\tau$  candidates. The anomalous  $\tau$  magnetic moment is measured to be  $a_\tau = 0.0009^{+0.0032}_{-0.0031}$ , while the electric dipole moment of the  $\tau$  lepton is measured to be  $-1.7 < d_\tau < 1.7 \times 10^{-17} e \text{ cm}$ .

## References

- [1] CMS Collaboration, "Search for exclusive or semi-exclusive photon pair production and observation of exclusive and semi-exclusive electron pair production in  $pp$  collisions at  $\sqrt{s} = 7 \text{ TeV}$ ", *JHEP* **11** (2012) 080, doi:10.1007/JHEP11(2012)080, arXiv:1209.1666.
- [2] CMS Collaboration, "Exclusive photon-photon production of muon pairs in proton-proton collisions at  $\sqrt{s} = 7 \text{ TeV}$ ", *JHEP* **01** (2012) 052, doi:10.1007/JHEP01(2012)052, arXiv:1111.5536.
- [3] J. Schwinger, "On quantum-electrodynamics and the magnetic moment of the electron", *Phys. Rev.* **73** (1948) 416, doi:10.1103/PhysRev.73.416.
- [4] R. H. Parker et al., "Measurement of the fine-structure constant as a test of the standard model", *Science* **360** (2018) 191, doi:10.1126/science.aap7706, arXiv:1812.04130.
- [5] X. Fan, T. G. Myers, B. A. D. Sukra, and G. Gabrielse, "Measurement of the electron magnetic moment", *Phys. Rev. Lett.* **130** (2023) 071801, doi:10.1103/PhysRevLett.130.071801, arXiv:2209.13084.
- [6] Muon g-2 Collaboration, "Measurement of the positive muon anomalous magnetic moment to 0.46 ppm", *Phys. Rev. Lett.* **126** (2021) 141801, doi:10.1103/PhysRevLett.126.141801, arXiv:2104.03281.

- [7] Muon g-2 Collaboration, “Measurement of the positive muon anomalous magnetic moment to 0.20 ppm”, *Phys. Rev. Lett.* **131** (2023) 161802, doi:10.1103/PhysRevLett.131.161802, arXiv:2308.06230.
- [8] L. Beresford and J. Liu, “New physics and tau  $g - 2$  using LHC heavy ion collisions”, *Phys. Rev. D* **102** (2020) 113008, doi:10.1103/PhysRevD.102.113008, arXiv:1908.05180. [Erratum: doi:10.1103/PhysRevD.106.039902].
- [9] S. Eidelman and M. Passera, “Theory of the tau lepton anomalous magnetic moment”, *Mod. Phys. Lett. A* **22** (2007) 159, doi:10.1142/S0217732307022694, arXiv:hep-ph/0701260.
- [10] Y. Yamaguchi and N. Yamanaka, “Large long-distance contributions to the electric dipole moments of charged leptons in the standard model”, *Phys. Rev. Lett.* **125** (2020) 241802, doi:10.1103/PhysRevLett.125.241802, arXiv:2003.08195.
- [11] M. Dyndal, M. Klusek-Gawenda, M. Schott, and A. Szczurek, “Anomalous electromagnetic moments of  $\tau$  lepton in  $\gamma\gamma \rightarrow \tau^+\tau^-$  reaction in Pb+Pb collisions at the LHC”, *Phys. Lett. B* **809** (2020) 135682, doi:10.1016/j.physletb.2020.135682, arXiv:2002.05503.
- [12] ATLAS Collaboration, “Observation of the  $\gamma\gamma \rightarrow \tau\tau$  process in Pb+Pb collisions and constraints on the  $\tau$ -lepton anomalous magnetic moment with the ATLAS detector”, *Phys. Rev. Lett.* **131** (2023) 151802, doi:10.1103/PhysRevLett.131.151802, arXiv:2204.13478.
- [13] CMS Collaboration, “Observation of  $\tau$  lepton pair production in ultraperipheral lead-lead collisions at  $\sqrt{s_{NN}} = 5.02$  TeV”, *Phys. Rev. Lett.* **131** (2023) 151803, doi:10.1103/PhysRevLett.131.151803, arXiv:2206.05192.
- [14] DELPHI Collaboration, “Study of tau-pair production in photon-photon collisions at LEP and limits on the anomalous electromagnetic moments of the tau lepton”, *Eur. Phys. J. C* **35** (2004) 159, doi:10.1140/epjc/s2004-01852-y, arXiv:hep-ex/0406010.
- [15] OPAL Collaboration, “An upper limit on the anomalous magnetic moment of the tau lepton”, *Phys. Lett. B* **431** (1998) 188, doi:10.1016/S0370-2693(98)00520-6, arXiv:hep-ex/9803020.
- [16] L3 Collaboration, “Measurement of the anomalous magnetic and electric dipole moments of the tau lepton”, *Phys. Lett. B* **434** (1998) 169, doi:https://doi.org/10.1016/S0370-2693(98)00736-9.
- [17] Belle Collaboration, “An improved search for the electric dipole moment of the  $\tau$  lepton”, *JHEP* **04** (2022) 110, doi:10.1007/JHEP04(2022)110, arXiv:2108.11543.
- [18] ARGUS Collaboration, “A search for the electric dipole moment of the tau lepton”, *Phys. Lett. B* **485** (2000) 37, doi:10.1016/S0370-2693(00)00630-4, arXiv:hep-ex/0004031.
- [19] ATLAS Collaboration, “Observation of photon-induced  $W^+W^-$  production in  $pp$  collisions at  $\sqrt{s} = 13$  TeV using the ATLAS detector”, *Phys. Lett. B* **816** (2021) 136190, doi:10.1016/j.physletb.2021.136190, arXiv:2010.04019.

- [20] CMS Collaboration, “Study of exclusive two-photon production of  $W^+W^-$  in  $pp$  collisions at  $\sqrt{s} = 7$  TeV and constraints on anomalous quartic gauge couplings”, *JHEP* **07** (2013) 116, doi:10.1007/JHEP07(2013)116, arXiv:1305.5596.
- [21] CMS Collaboration, “Evidence for exclusive  $\gamma\gamma \rightarrow W^+W^-$  production and constraints on anomalous quartic gauge couplings in  $pp$  collisions at  $\sqrt{s} = 7$  and 8 TeV”, *JHEP* **08** (2016) 119, doi:10.1007/JHEP08(2016)119, arXiv:1604.04464.
- [22] CMS and TOTEM Collaborations, “Observation of proton-tagged, central (semi)exclusive production of high-mass lepton pairs in  $pp$  collisions at 13 TeV with the CMS-TOTEM precision proton spectrometer”, *JHEP* **07** (2018) 153, doi:10.1007/JHEP07(2018)153, arXiv:1803.04496.
- [23] ATLAS Collaboration, “Measurement of exclusive  $\gamma\gamma \rightarrow W^+W^-$  production and search for exclusive Higgs boson production in  $pp$  collisions at  $\sqrt{s} = 8$  TeV using the ATLAS detector”, *Phys. Rev. D* **94** (2016) 032011, doi:10.1103/PhysRevD.94.032011, arXiv:1607.03745.
- [24] CMS Collaboration, “The CMS experiment at the CERN LHC”, *JINST* **3** (2008) S08004, doi:10.1088/1748-0221/3/08/S08004.
- [25] CMS Collaboration, “Performance of the CMS Level-1 trigger in proton-proton collisions at  $\sqrt{s} = 13$  TeV”, *JINST* **15** (2020) P10017, doi:10.1088/1748-0221/15/10/P10017, arXiv:2006.10165.
- [26] CMS Collaboration, “The CMS trigger system”, *JINST* **12** (2017) P01020, doi:10.1088/1748-0221/12/01/P01020, arXiv:1609.02366.
- [27] H.-S. Shao and D. d’Enterria, “gamma-UPC: automated generation of exclusive photon-photon processes in ultraperipheral proton and nuclear collisions with varying form factors”, *JHEP* **09** (2022) 248, doi:10.1007/JHEP09(2022)248, arXiv:2207.03012.
- [28] J. Alwall et al., “The automated computation of tree-level and next-to-leading order differential cross sections, and their matching to parton shower simulations”, *JHEP* **07** (2014) 079, doi:10.1007/JHEP07(2014)079, arXiv:1405.0301.
- [29] J. Alwall et al., “MadGraph/MadEvent v4: the new web generation”, *JHEP* **09** (2007) 028, doi:10.1088/1126-6708/2007/09/028.
- [30] R. Frederix and S. Frixione, “Merging meets matching in MC@NLO”, *JHEP* **12** (2012) 061, doi:10.1007/JHEP12(2012)061, arXiv:1209.6215.
- [31] L. A. Harland-Lang, M. Tasevsky, V. A. Khoze, and M. G. Ryskin, “A new approach to modelling elastic and inelastic photon-initiated production at the LHC: SuperChic 4”, *Eur. Phys. J. C* **80** (2020) 925, doi:10.1140/epjc/s10052-020-08455-0, arXiv:2007.12704.
- [32] I. Brivio, Y. Jiang, and M. Trott, “The SMEFTsim package, theory and tools”, *JHEP* **12** (2017) 070, doi:10.1007/JHEP12(2017)070, arXiv:1709.06492.
- [33] I. Brivio, “SMEFTsim 3.0 — a practical guide”, *JHEP* **04** (2021) 073, doi:10.1007/JHEP04(2021)073, arXiv:2012.11343.

- [34] P. Artoisenet, V. Lemaître, F. Maltoni, and O. Mattelaer, “Automation of the matrix element reweighting method”, *JHEP* **12** (2010) 068, doi:10.1007/JHEP12(2010)068, arXiv:1007.3300.
- [35] P. Nason, “A new method for combining NLO QCD with shower Monte Carlo algorithms”, *JHEP* **11** (2004) 040, doi:10.1088/1126-6708/2004/11/040, arXiv:hep-ph/0409146.
- [36] S. Frixione, P. Nason, and C. Oleari, “Matching NLO QCD computations with parton shower simulations: the POWHEG method”, *JHEP* **11** (2007) 070, doi:10.1088/1126-6708/2007/11/070, arXiv:0709.2092.
- [37] S. Alioli, P. Nason, C. Oleari, and E. Re, “A general framework for implementing NLO calculations in shower Monte Carlo programs: the POWHEG BOX”, *JHEP* **06** (2010) 043, doi:10.1007/JHEP06(2010)043, arXiv:1002.2581.
- [38] S. Alioli et al., “Jet pair production in POWHEG”, *JHEP* **04** (2011) 081, doi:10.1007/JHEP04(2011)081, arXiv:1012.3380.
- [39] S. Alioli, P. Nason, C. Oleari, and E. Re, “NLO Higgs boson production via gluon fusion matched with shower in POWHEG”, *JHEP* **04** (2009) 002, doi:10.1088/1126-6708/2009/04/002, arXiv:0812.0578.
- [40] T. Sjöstrand et al., “An introduction to PYTHIA 8.2”, *Comput. Phys. Commun.* **191** (2015) 159, doi:10.1016/j.cpc.2015.01.024, arXiv:1410.3012.
- [41] CMS Collaboration, “Extraction and validation of a new set of CMS PYTHIA8 tunes from underlying-event measurements”, *Eur. Phys. J. C* **80** (2020) 4, doi:10.1140/epjc/s10052-019-7499-4, arXiv:1903.12179.
- [42] R. D. Ball et al., “Unbiased global determination of parton distributions and their uncertainties at NNLO and at LO”, *Nucl. Phys. B* **855** (2012) 153, doi:10.1016/j.nuclphysb.2011.09.024, arXiv:1107.2652.
- [43] NNPDF Collaboration, “Parton distributions with QED corrections”, *Nucl. Phys. B* **877** (2013) 290, doi:10.1016/j.nuclphysb.2013.10.010, arXiv:1308.0598.
- [44] NNPDF Collaboration, “Parton distributions from high-precision collider data”, *Eur. Phys. J. C* **77** (2017) 663, doi:10.1140/epjc/s10052-017-5199-5, arXiv:1706.00428.
- [45] GEANT4 Collaboration, “GEANT4 — a simulation toolkit”, *Nucl. Instrum. Meth. A* **506** (2003) 250, doi:10.1016/S0168-9002(03)01368-8.
- [46] CMS Collaboration, “Particle-flow reconstruction and global event description with the CMS detector”, *JINST* **12** (2017) P10003, doi:10.1088/1748-0221/12/10/P10003, arXiv:1706.04965.
- [47] CMS Collaboration, “Electron and photon reconstruction and identification with the CMS experiment at the CERN LHC”, *JINST* **16** (2021) P05014, doi:10.1088/1748-0221/16/05/P05014, arXiv:2012.06888.
- [48] CMS Collaboration, “ECAL 2016 refined calibration and Run2 summary plots”, CMS Detector Performance Summary CMS-DP-2020-021, 2020.



- [49] CMS Collaboration, “Performance of the CMS muon detector and muon reconstruction with proton-proton collisions at  $\sqrt{s} = 13$  TeV”, *JINST* **13** (2018) P06015, doi:10.1088/1748-0221/13/06/P06015, arXiv:1804.04528.
- [50] CMS Collaboration, “Performance of reconstruction and identification of  $\tau$  leptons decaying to hadrons and  $\nu_\tau$  in pp collisions at  $\sqrt{s} = 13$  TeV”, *JINST* **13** (2018) P10005, doi:10.1088/1748-0221/13/10/P10005, arXiv:1809.02816.
- [51] CMS Collaboration, “Identification of hadronic tau lepton decays using a deep neural network”, *JINST* **17** (2022) P07023, doi:10.1088/1748-0221/17/07/P07023, arXiv:2201.08458.
- [52] CMS Collaboration, “Performance of missing transverse momentum reconstruction in proton-proton collisions at  $\sqrt{s} = 13$  TeV using the CMS detector”, *JINST* **14** (2019) P07004, doi:10.1088/1748-0221/14/07/P07004, arXiv:1903.06078.
- [53] CMS Collaboration, “Description and performance of track and primary-vertex reconstruction with the CMS tracker”, *JINST* **9** (2014) P10009, doi:10.1088/1748-0221/9/10/P10009, arXiv:1405.6569.
- [54] CMS Tracker Group Collaboration, “The CMS phase-1 pixel detector upgrade”, *JINST* **16** (2021) P02027, doi:10.1088/1748-0221/16/02/P02027, arXiv:2012.14304.
- [55] CMS Collaboration, “Track impact parameter resolution for the full pseudo rapidity coverage in the 2017 dataset with the CMS phase-1 pixel detector”, CMS Detector Performance Summary CMS-DP-2020-049, 2020.
- [56] CMS Collaboration, “Precision luminosity measurement in proton-proton collisions at  $\sqrt{s} = 13$  TeV in 2015 and 2016 at CMS”, *Eur. Phys. J. C* **81** (2021) 800, doi:10.1140/epjc/s10052-021-09538-2, arXiv:2104.01927.
- [57] CMS Collaboration, “CMS luminosity measurement for the 2017 data-taking period at  $\sqrt{s} = 13$  TeV”, CMS Physics Analysis Summary CMS-PAS-LUM-17-004, 2018.
- [58] CMS Collaboration, “CMS luminosity measurement for the 2018 data-taking period at  $\sqrt{s} = 13$  TeV”, CMS Physics Analysis Summary CMS-PAS-LUM-18-002, 2019.
- [59] R. Barlow and C. Beeston, “Fitting using finite Monte Carlo samples”, *Comput. Phys. Commun.* **77** (1993) 219, doi:10.1016/0010-4655(93)90005-W.
- [60] CMS Collaboration, “Measurement of the inelastic proton-proton cross section at  $\sqrt{s} = 13$  TeV”, *JHEP* **07** (2018) 161, doi:10.1007/JHEP07(2018)161, arXiv:1802.02613.